# 3D Coil Setup as a tool for MR sensor characterization

**Mathieu Da Silva Pais Correia**

Thesis to obtain the Master of Science Degree in

## Bioengineering and Nanosystems

Supervisor: Prof. Susana Isabel Pinheiro de Cardoso Freitas

### Examination Committee:

Chairperson: Prof. Jorge Manuel Ferreira Morgado

Supervisor: Prof. Susana Isabel Pinheiro de Cardoso Freitas

Members of the Committee: Dr. Mustafa Erkovan

**October 2021**

# Preface

The work presented in this thesis was performed at the INESC-MN institute of Instituto superior Técnico (Lisbon, Portugal), during the period September-October 2021, under the supervision of Prof. Susana Isabel Pinheiro de Cardoso Freitas.

# Declaration

I declare that this document is an original work of my own authorship and that it fulfills all the requirements of the Code of Conduct and Good Practices of the Universidade de Lisboa.

# Acknowledgements

Firstly, I would like to show my appreciation to the entire INESC-MN's workers for the incredible flexibility and constant support throughout the year. Starting in the fix all types of problems Natércia Correia; to Engineer Fernando Silva for the steadiest hands in the building; to Fabian Näf for being the executive Co-Producer of this Thesis; to Pedro Araújo for all the very specific brilliant inputs; to Pedro Ribeiro for answering me to every broad question I had; to Marília Silva for being there for me every step of the way; and finally to Professor Susana Freitas for being able to create an "expect not to expect so that you'll never stop trying", kind of environment.

Additionally, I would like to thank my family for all the generated love that made this not so easy task we call an education a little less heavy and a little more brighter. Thank you, Mom and Dad, for being home every time I went, thank you Sylvie, for your kind and gentle hearth and Charlie and Patricia, thank you for you and for allowing me to simply be me, and finally, thank you to Lucas and Alice for your unconditional love and for the sweet reminder of total absolute genuinity.

Lastly, thank you to all my friends, because you know, I know, you know.

# Abstract

To this end, the present work consists of assembling several MR sensors, including one that composes the three spatial dimensions, enabling us to have multiaxial magnetic sensing.

In addition, a 3D Helmholtz coil setup that could create a specific magnetic field in an arbitrary magnetic direction was fabricated to allow the subsequent characterization of the assembled sensor. This type of device doesn't yet exist at INESC-MN facilities, disabling this type of precise 3D sensor characterization.

Moreover, our set of sensors was characterized regarding there, MR curves, noise spectrum, detectivity, and low field AC magnetic field detection. Which means this device leads also to new types of sensor characterization, that weren't previously available.

For our MR curves, every sensor produced coherent data compared to the MR curves produced by the 140 Oe setup. Our best match was with the MTJ's given by INESC-MN, showing a disparity regarding the sensor's sensitivity and magnetoresitivity of less than 1%.

The best detectivity was measured on our 3D Magnetometer and showed values of 7.03 nT/√Hz, 6.57 nT/√Hz, and 7.11 nT/√Hz for the X, Y, and Z-axis, respectively.

All sensors were able to detect a low-frequency AC field produced by our 3D Coil Setup. The estimated root means square value for an AC magnetic field oscillating at a 10 Hz frequency was 9.27 nT for an SNR of 1 for the X-axis of our Magnetometer. This produces a real result of our sensor limiting detectivity's, which were able to be characterized with the measurement of the sensor noise spectrum with the introduction of an actual magnetic field.

We linearized our Spin Valve sensor, which was our most sensitive sensor, using cross magnetic fields applied in our 3D Coil Setup, obtaining a 93% and 30% reduction in sensitivity and coercivity, respectively.



**Keywords:** Magnetoresistive, Magnetic Tunnel Junction, Spin-Valve, Detectivity, Helmholtz Coil, Magnetometer

# Resumo

Para este efeito, este trabalho consiste na montagem de vários sensores Magnetoresistivos, incluindo um que seja capaz de detetar um campo magnético nas três dimensões espaciais.

Alem disto, um dispositivo composto por três ortogonais bobinas de Helmholtz foi criado com o objetivo de gerar um campo magnético arbitrário nas três dimensões espaciais, para subsequentemente podermos caracterizar o nosso conjunto de sensores. Este tipo de dispositivo ainda não existe nas instalações do INESC-MN, o que impossibilita a caracterização precisa de magnetómetros tridimensionais.

O nosso conjunto de sensores foi caracterizado em relação a sua curva magnetoresistiva, espectro de ruido, detetividade e a deteção de campos magnéticos de corrente alternada de baixa frequência. Consequentemente, este dispositivo leva a novos tipos de caracterização, que previamente não eram possíveis.

Respetivamente as nossas curvas magnetoresistivas, todos os sensores produziram dados coerentes comparando com as curvas produzidas pelo setup 140 Oe. Das nossas curvas, os sensores que produziram uma melhor coincidência de dados foram, respetivamente, as MTJ's dadas pelo INESC-MN, que mostraram uma disparidade em relação a sensibilidade e a sua magnetoresistividade de menos de 1%.

A nossa melhor detetividade foi detetado pelo nosso Magnetómetro Tridimensional, que mostrou valores de 7.03 nT/√Hz, 6.57 nT/√Hz, and 7.11 nT/√Hz para o nosso eixo do X, Y e Z, respetivamente.

Todos os nossos sensores conseguiram detetar campos magnéticos de corrente alternada de baixa frequência induzido pelo nosso dispositivo de bobinas tridimensionais. O estimado valor quadrático medio para um campo magnético oscilando a 10 Hz, seria de 9.27 nT para uma razão de SNR equivalente a 1 no eixo do X do nosso magnetómetro tridimensional. Este tipo de caracterização produz um resultado real dos limites de detetividade do nosso sensor, pelo simples facto de medir o ruido com a indução de um campo magnético na região de interesse do sensor.

Alem de mais, usando o nosso setup para induzir campos cruzados num das nossas spin-valves, que consiste num dos nossos sensores com maior sensibilidade. Conseguimos obter uma redução de 93% e de 30% em relação a nossa sensibilidade e a nossa coercividade, respetivamente.

**Palavras-Chaves:** Magnetoresistivdade, Magnetic Tunnel Junction, Detetividade, Helmholtz Coil, Spin-Valve, Magnetómetro

# Content

# List Of Images

# List of abbreviations

MR ...…….…… Magnetoresistive

AMR ……... Anisotropic Magnetoresistance

TMR ……... Tunnel Magnetoresistance

GMR ……... Giant Magnetoresistance

PMA …… Perpendicular Magnetic Anisotropy

FM ..……. Ferromagnetic

3D …… Three-Dimensional

MTJ ……. Magnetic Tunnel Junction

SV …….. Spin-Valve

RMS ……..... Root Mean Square

SNR ……..... Signal To Noise Ratio

RBW ……... Resolution Bandwidth

MEMS ……. Microelectromechanical System

AC ……..... Alternate Current

# Chapter 1

## Introduction

### Motivation

The data storage market was revolutionized by MR Sensors, which allowed the recording industry to display a substantial increase in storage density and data longevity [1]. MR sensors came to give attractive propositions to other fields of study, for instance, ABS sensors (automotive market) [2]. In addition, their ability to detect weak magnetic fields at room temperature started to be used in other applications, for instance, sensors for biomolecular recognition and compasses in mobile phones [3]. Moreover, the detection of low-frequency alternate currents by MR Sensors has some interesting applications in the field of human healthcare (20-300 Hz), geological investigation (0.01-5 Hz), and magnetic anomaly detection (0.04-2 Hz) [4]. Allied to the capability of being microfabricated at substantially high rates, MR sensors are optimal choices for several applications.

Tunnel MR sensors are one of the most forthcoming sensors in spintronics devices due to their high MR ratios, great detectivity in the low-frequency limit [3], and CMOS compatibility [5]. Currently, MR sensors, although capable of fulfilling a wide variety of demands, are limited to sensing a single component of an external magnetic field. Propositions with the complete 3D sensing integration lack compactness, sensitivity, and detectivity. This type of sensor with multiaxial sensing would substantially benefit industrial and biomedical diagnostic techniques for the robotic sensing industry, making the current investigation and research considerably beneficial. As a result of this vast potential, the INESC-MN spintronic department has been studying and investigating these types of MR sensors for a while now. This creates a need for a device that could accurately characterize a 3D Magnetometer in all sensing directions, such as a portable setup of a 3D Helmholtz Coil.

In addition, this device could lead to some new types of sensor characterization being available at INESC-MN, such as the effect of linearization of cross magnetic fields throughout MR sensors and the measurement of a sensor's capability on detecting low-frequency alternate currents magnetic fields.

### State-of-the-art

Initially, the concept behind Magnetometer came from Germany, from a scientist named Carl Friedrich Gauss, in 1882. The device consisted of a permanent magnet suspended in midair by a fiber [6]. Since then, several magnetometers have been designed, being the fluxgate sensor, one of the preeminent

ones. The main principle behind fluxgate sensors is Faraday's Law of induction. As shown below, we have a FM core material with two coils, an excitation, and a sense coil [7].

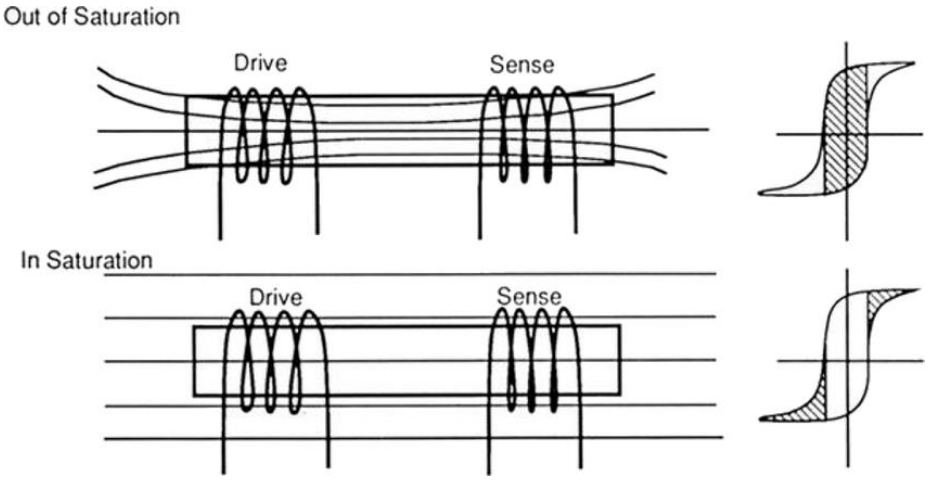


*Figure 1 - Theoretical background definition of saturated and non-saturated fluxgate sensor*

The current in the excitation coil drives the soft magnetic material to be periodically saturated in both polarities. Consequently, it will induce a change in the core permeability regarding unsaturated and saturated states. The sensing coil measures the flux change in the material core by measuring the voltage induced in it [7].

Although fluxgates are used in various applications and present resolutions that can reach 10-pT, they present disadvantages such as power consumption and several pT/√Hz noise densities in the low-frequency regime [8]. Some of these disadvantages began to be surpassed with MR sensors, coupled with the fact that they could be integrated with CMOS technology, which made them witness a rapid growth curve [9].

Magnetoresistance was discovered in 1857 by William Thomson, where he noted that the resistance of a magnetic material changed when subjected to an external magnetic field [8] [10] [11]. MR sensors can be classified nowadays in one of three operating principles, TMR, GMR or AMR.

AMR is based on the intrinsic magnetoresistance of our FM material. It has been a building foundation to build our MR sensors based on the spontaneous resistance anisotropy of our material according to the presence or non-presence of an external magnetic field [12]. AMR sensors present dynamic ranges in the order of hundreds of uT and resolutions in the order of 1 nT, detectivities in the order of nT/√Hz for frequencies higher than 10 Hz, and sensitivities in order of 10 mV/mT.

The GMR effect is based on a multilayered structure that improved spintronics devices and sensitivity. For instance, considering a NiFeCo/Cu/Co/Cu multilayer, where between 0 and 50 Oe, a variation in resistance of 16% was able to be observed [13]. In contrast with AMR, GMR devices have higher hysteresis, up to 10% [14], and are more used for reading heads in magnetic recording systems.

Although with some biasing mechanisms, good sensing properties and repeatability can be achieved. This will, however, result in higher power consumption.

Although based on a similar approach to the GMR effect, TMR has the current flowing through the device interface based on a quantum mechanical effect. The spacer in TMR is an insulator barrier, as opposed to a conductive non-magnetic spacer in GMR. The TMR ratio has been continuously enhanced, reaching in 2004, by S.S. Parkin et al. in IBM Almaden and S. Yuasa et al. in Japan, MR ratios of 220% with MTJ's of CoFe/MgO layers [15] [16]. In 2008, Ikeda et al. reported a magnetoresistance of 604% at 300 K with MTJ's of CoFeB/MgO/CoFeB [17].

The standard tunnel MR sensor, MTJ's, has a free layer defined along the easy axis of magnetization of the FM material, in the case of in-plane sensing. Alternatively, the easy axis of magnetization can be defined perpendicularly to the sensor plane, enabling us to have magnetic sensors sensitive to the Z direction. Sensitivities for in-plane sensing, can be as high as 2000-4000%/mT [18] [19]. However, sensitivities for out-of-plane sensing have only reached 4%/mT [20], which brings a vast disparity between the sensitivity of in-plane and out-of-plane sensing, complicating the integration of these sensors in a 3D magnetometer.

One approach for nanofabricating a MTJ sensitive to the out-of-plane direction is to build an MTJ with an ultrathin free layer exploiting the interfacial perpendicular magnetic anisotropy (PMA) between the two CoFeB and MgO layers [21]. Such PMA contribution increases with decreasing CoFeB thickness. Consequently, this will allow our sensor to have an out-of-plane magnetization, ultimately sensitive to our magnetic field's Z-component. Let et al. have shown for MTJ's consisting in a stack of CoFeB/MgO/CoFeB that using an ultra-thin reference layer, 1.2 nm, the free layer was able to rotate out-of-plane when a perpendicular magnetic field is applied, achieving a sensitivity of 3%/mT [22]. In 2019, Zicong Lei et al. tested several MTJ to discover the optimal free layer thickness to maximize the TMR ratio for out-of-plane sensing [23]. They build a MTJ's with a pinned perpendicular antiferromagnetic layer, based on (Co/Pt) multilayers to provide a high perpendicular magnetic energy and wide exchange coupling field [25, 26]. The optimal TMR ratio for the free layer thickness was measured at 1.6 nm [23].

A second approach to nanofabricate a MTJ sensitive to the out-of-plane direction is to bend the magnetic flux lines towards the in-plane direction, taking advantage of flux concentrators incorporated inside our sensor. A general approach is to develop a three-axis magnetometer with four GMR cells to form a Wheatstone bridge mounted around a flux concentrator. For X and Y directions, the flux lines are bent parallel to the sensing axis of the GMR cell. The magnetic flux is redirected from the out-of-plane direction to the in-plane direction for Z magnetic sensing, allowing the GMR cell to detect the Z-axis naturally [24]. The GMR cells could be switched to integrate MTJ's, which could enhance the detectability. This was done, in 2015, by James G Deak, where he placed a series of permalloy bars over an array of MTJ. When a magnetic field was applied parallel to the Z-Axis, the flux was drawn to the permalloy bars and deviated into the negative and positive X-Direction. By adjusting the sensor geometry and MTJ, they achieved a sensitivity between 0.2 mV/V/Oe and 3 mV/V/Oe with saturation

fields ranging from 1000 Oe to less than 50 Oe [25]. However, this can present difficulties due to the development of the flux concentrator and the device design arrangement.

A third and last option is to set an in-plane sensor up as a perpendicular field sensor since MTJ's naturally sense in-plane magnetic fields. The most trivial approach for fabricating a Z-axis magnetic field sensor is to tilt the MTJ on its side mechanically. This can be done in two ways: by tilting the sensor chip on its side or mounting the sensor in a SIP style packaging. These approaches are large and relatively expensive. [25]

MEMS magnetic sensors have often been characterized using a Helmholtz Coil, an inexpensive way of inducing a uniform magnetic field that can easily change and be tuned to whatever magnetic window we need for our given sensors. Different techniques can do the calibration of the Helmholtz Coil. For instance, in the past, a standard magnet could be used to perform these calibrations. Another alternative is to use a hall probe sensor that is easier and has a more accurate calibration.

A 3D Helmholtz coil system can be implemented to create and generate a controlled 3D magnetic field with arbitrary and well-defined orientation. Therefore, allowing the characterization of 3D Magnetometers in a more precise and controlled environment.

## Thesis Outline and Goals

The goal of this Thesis is to assemble and mount a fully functional 3D magnetometer using an array of MTJ's composed of a chip carrier with a maximum size of 100 $\mathrm{mm}^2$ and with the final device dimension no bigger than 25 $\mathrm{cm}^2$. Followed by the subsequent fabrication of a setup of three orthogonal Helmholtz coils to provide an adequate 3D magnetic field, inside the pT range, to fully characterize a set of sensors, including the 3D Magnetometer.

This stated this Thesis is organized in the following way:

In Chapter 2 a theoretical background of MR sensors and Helmholtz Coils is presented.

In Chapter 3 the experimental techniques available at INESC-MN facilities and used in this work are briefly explained.

In Chapter 4 the fabrication process for the 3D Helmholtz Coil is explained.

In Chapter 5 the assembling of the 3D Magnetometer is explained.

In Chapter 6 the MR and noise characterization of our dataset of sensors is presented.

In Chapter 7 the magnetic AC low field detection of our dataset of sensors is presented.

In Chapter 8 the result of crossed applied magnetic fields in one of our sensor's MR curve is presented.

In Chapter 9 the conclusion is presented

# Chapter 2

## Theoretical Background

### 2.1 MR Sensors

MR sensors core rises from the exploitation of the magnetic properties of FM material. The FM material can exhibit spontaneous magnetization, a net magnetic moment in the absence of an external magnetic field. The exchange interaction, which controls the sharing of orbitals between valence electrons according to their spin, is more significant in FM materials, allowing magnetic spins to be all aligned together, forming one giant magnetic domain.

MR sensors are based on the MR effect that describes the change in the material's electric resistance according to its magnetization, which can be changed with the assist of an external magnetic field. By sweeping the magnetic field while measuring the change in electrical resistance, we can obtain a Rmax (Maximum Resistance) and Rmin (Minimum Resistance), that respectively, allows us to calculate the magnitude of this MR effect, that is what we know as magnetoresistance:

$$MR(\%) = \frac{Rmax - Rmin}{Rmin} * 100 \quad (1)$$

There are three principal types of MR sensors based on different physical effects, mechanisms, and features, respectively: the AMR, the GMR, and the TMR.

#### 2.1.1 AMR

The AMR effect was discovered in 1857 by lord kelvin in 3d transition metals and their alloys [26]. This effect is described by the change in electrical resistance regarding the orientation of the material's magnetization. For most materials, when current and magnetization are parallel (higher probability of electron scattering), we have a higher resistance than in the reverse situation.

The resistivity, $\rho$, has a dependence on the angle between the current and the magnetization, $\Theta$, being described as:

$$\rho = \rho \perp + (\rho // - \rho \perp)\cos^2(\Theta) \quad (2)$$

With $\rho \perp$ and $\rho //$ being the minimum and maximum resistivity state, respectively.

We observe in thin films that there is a threshold for AMR set at 3%. Although the AMR depends on various factors, such, alloy composition, film thickness, substrate, deposition rate, and others, we rarely go beyond this obtained magnetoresistance [27].

### 2.1.2 GMR

The GMR is a quantum mechanical effect that finds that in layered magnetic structures, the resistivity depends on the relative alignment of the magnetizations of adjacent FM layers [27]. This phenomenon is due to spin-dependent electron scattering and was first discovered in 1988 by Baibich when he noted that for a specific multilayered structure, Fe/Cr/Fe multilayers, the magnetoresistance decreased more than 50% when the magnetization direction of both Fe layers, where parallelly aligned, coming from a state of antiparallel magnetization due to the antiferromagnetic interchange coupling at zero field [12]. The switch of the orientation of our magnetic domains was obtained by applying an external magnetic field. This pioneer experiment is displayed in the image below [12].

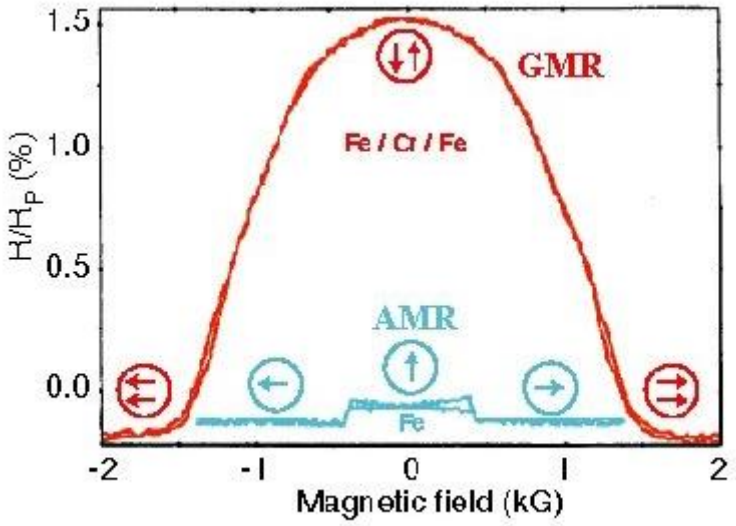


*Figure 2 - Result of experiment comparing the MR difference between AMR and GMR [12]*

The blue curve shows the AMR effect of a 250 A Fe layer for comparison. The typical value for magnetoresistance in GMR devices at room temperature is 10-20%, a significant difference compared to AMR [12].

The multilayer where we can observe this GMR effect is composed of two FM layers separated by a conductive non-magnetic metallic layer (spacer). The electrical resistance will vary between a minimum and a maximum, according to the relative orientation of the magnetization of the FM Layers.

The GMR effect is due to the spin polarization of the electrons, working as a polarizer. This discovery of the spin filtering effect opened new ways and fields of research, such as spintronics.

To understand the GMR effect, we can assume Mott's current model [28], which assumes two independent current channels for spin-up and spin-down electrons. For each channel, the scattering process in the case of antiparallel alignment will scatter at the same rate across each interface. Whereas, for parallel alignment, the structure ceases to be symmetric, which will allow the electrons that have a spin aligned with the magnetic orientation to freely move around the structure, causing a short circuit effect and being responsible for almost entirely all the conduction current, hence lowering the overall resistance [29]. In conclusion, the resistance will be lower for a parallel magnetic moment than with an antiparallel alignment.

This could be illustrated by the following exemplificative state diagram:

0

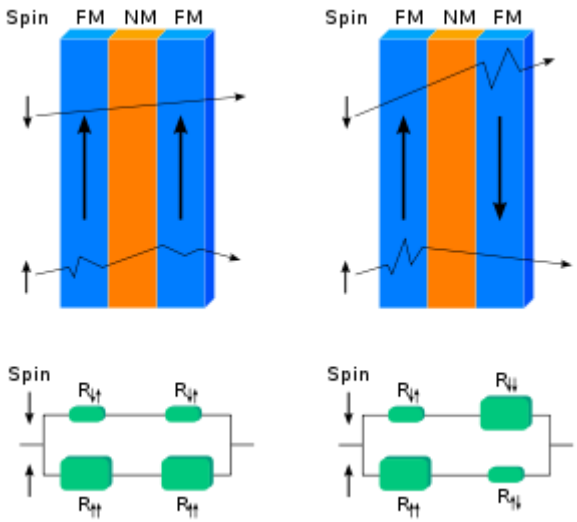


*Figure 3 - Spin alignment and misalignment with the magnetic structure orientation, inducing a difference in resistance*

One major problem regarding GMR was that even though the magnetoresistance was more significant, the sensitivities of AMR sensors were still better than GMR sensors. To improve this sensitivity issue, in 1991, Dieny and Co-Workers proposed a new type of GMR structure, called spin-valve [30].

In spin-valves, one of the most advanced and used GMR sensors, we have each of the FM layers separated by a magnetic spacer. We have an antiferromagnetic layer adjacent to one of the FM layers. This antiferromagnet goal is to pin the FM magnetization to a fixed orientation magnetization, respectively, a fixed layer, to be used as a reference against a free-layer magnetization that is left free to be aligned with an externally applied field, which will allow the free layer to rotate between a parallel state and an antiparallel state relative to the magnetization of the fixed layer [12]. These two states, regarding electrical resistance, show a vast difference between them, providing an excellent readout of the magnetization state of the device. The non-magnetic spacer is where the electric transport reacts to the relative direction of the free layer, where electron scattering will be oriented according to spin orientation (spin-up or spin-down) [12].

CoFe and NiFe are usually good choices for ferromagnet; due to their high MR and soft magnetic properties, Cu is usually chosen to be the magnetic spacer.

### 2.1.3 TMR

More recently, a new type of magnetoresistance emerged, TMR. It was based on the GMR effect. However, instead of having the two FM layers separated by a non-magnetic spacer, it was separated by an insulating layer, usually, AlOx or MgO (typically 4 – 30 A), which acts as a very efficient spin filter [10]. Moreover, instead of scattering electrons, we have tunnelling electrons around the thin insulator layer. This tunnelling is based on an exponentially decaying function of the electron wavelength, strictly a quantum mechanical phenomenon not contemplated by classical physics. Meservey and Tedrow [31] discovered this effect while doing some spin-dependent tunnelling experiences.

Once again, the magnetization of one of the FM layers is pinned while the other FM layer is free to align with the external magnetic field. The electrical resistance is higher when our FM layers are aligned antiparallelly.

In 1975 Jullière proposed a model to explain the electron tunnelling between two FM layers separated by a thin insulator barrier [32]. This was based on two hypotheses; the first is that the electrons are only able to tunnel between states of equal spin in the two FM layers, which means electrons originating from one spin state of the first FM layer can only be accepted by unfilled states of the same spin, from the second FM layer; the second hypothesis is that the tunnelling is proportional to the product between the density of states in the first and second ferromagnet [32] .

This is given by:

$$\mathrm{JP} \propto \mathrm{D1}(\uparrow)\,\mathrm{D2}(\uparrow) + \mathrm{D1}(\downarrow)\,\mathrm{D2}(\downarrow) \tag{3}$$

$$\mathrm{JPA} \propto \mathrm{D1}(\uparrow)\,\mathrm{D2}(\downarrow) + \mathrm{D1}(\downarrow)\,\mathrm{D2}(\uparrow) \tag{4}$$

JP and JPA are respectively the current density in the parallel and the antiparallel state, where Di (↑) and Di (↓) represent the spin-up and spin-down density of states for both our FM layers [32]. There is a strong spin imbalance at their Fermi level for FM material, resulting in a different number of available states for each spin band. For parallel alignment between the ferromagnets, the electrons of one spin constitute the majority. They can tunnel to the other electrode, where most of the density of states also corresponds to the same spin. On the other hand, in Figure 4, the density of states to receive spin-up electrons are constitute the majority in the first ferromagnet. In contrast, the other ferromagnet holds a

more significant density of states to receive spin-down electrons, increasing resistance, in the case of antiparallel alignment [32].

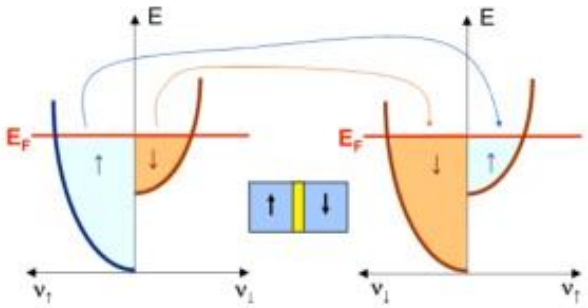


*Figure 4 - Electron tunnelling explanation from different density of states and electric predisposition to receive spin-up or spin-down electrons, regarding antiparallel magnetic conformations*

From this, we can rephrase the expression for magnetoresistance:

$$TMR = \frac{JP - JPA}{JP} * 100 \quad (4)$$

Were $JP$ is the density of states for parallel alignment and $JPA$ is for the case of antiparallel alignment.

We can also rewrite this equation, taking into consideration the polarization of spins in each FM layer [32]. Respectively the spin polarizations for left and right electrodes:

$$P\ 1{,}2 = D1{,}2(\uparrow) - \mathrm{D}1{,}2(\downarrow) \,/\, \mathrm{D}1{,}2(\uparrow) + \mathrm{D}1{,}2(\downarrow) \quad (5)$$

Being $D1{,}2(\uparrow)$ the spin polarization for spin up electrons and $\mathrm{D}1{,}2(\uparrow)$ for the spin-down electrons.

Rewriting the TMR expression and achieving the Landée formula:

$$TMR = 2P1 * P2/1 - P1 * P2 \quad (6)$$

Where P1 and P2 and respectively the polarization for each FM layer.

From this, we can conclude that materials with more significant spin imbalance, like Ni, Co, and Fe alloys, will achieve higher TMR ratios.

Jullière's model is oversimplified, and over the years, it has been further elaborated. However, there is a common factor in every model explaining the electron tunnelling between FM layers separated by an insulator. The magnitude of the tunnelling current is related to the overlap of the exponentially decaying wave function inside the barrier. Therefore, the current exponentially decreases with the increase in barrier thickness.

While TMR ratios have been increasing over the years, they still have not reached the theoretical predictions, which means there is still room to grow.

## 2.2 Magnetic Tunnel Junctions

As we previously mentioned, an MTJ stack consists of two FM layers, one free and one pinned, separated by an insulating barrier. The free layer is left free to be aligned with the external magnetic field, while the pinned layer is fixed by an exchange bias with an antiferromagnet that serves as the reference direction. In addition, we have a buffer layer and a capping layer that compose the full MTJ stack. Bellow follows a discriminative description of each layer and their respective functionalities [33].

**Buffer** The primary purpose of this layer is to allow the continued growth of continuous thin films for the barrier. To allow this growth, our buffer must provide a low resistance contact to our junction. Therefore, our buffer must have low resistivity and low interface roughness. Ta and Ru alternate layers are usually used.

**Free Layer** The free layer consists of the sensor response. The magnetization aligns with the external magnetic field, which will change the electrical resistance of our MTJ, which we intend to measure. FM materials used for tunnel junctions are magnetic transition metals like Ni, Fe, Co, and their alloys. These metals have a high polarization to maximize our TMR ratio and a low coercivity to allow magnetization reversal. Amorphous CoFeB ferromagnets have been exploited in spintronic devices and shown larger TMR ratios than CoFe ferromagnets [35].

**Insulating Layer** The insulating layer must be a non-magnetic oxide to prevent spin-flip events in the tunnelling process while maintaining the integrity of the FM layers. To ensure the conduction through electron tunnelling, the thickness needs to be below 20 A, and the film needs to be continuous.

**Pinned and Reference layers:** The free layer can rotate freely according to an external magnetic field, while the reference layer should not rotate under this influence. This can be achieved by applying an exchange bias with an antiferromagnet to force the adjacent FM layer to remain fixed for a specific range of fields. A second strategy is to deposit more layers, using magnetic principles such as RKKY (Ruderman-Kittel-Kasuya-Yosida) between two ferromagnets with a spacer in between. Therefore, successive FM layers will be ferromagnetically or antiferromagnetically coupled, depending on the thickness of the spacer. The pinned layer is coupled to an antiferromagnet to pin the magnetization of the adjacent FM layer [34]. Meanwhile, the other FM layer is called the reference layer, both separated by a non-magnetic spacer.

**Cap Layer** This layer consists in preventing oxidation of the underlying metallic layers.

## 2.3 Spin-Valves

Spin-Valves, as mentioned previously, consists of two FM layers with a non-magnetic spacer between them. In Spin-Valves, the free layer is left free to align with the external applied magnetic field.

The stack for Spin-Valves devices is very similar to the one observed above. The only significant difference is the non-magnetic spacer that is used instead of the thin insulator barrier. A typical spacer to be used is Cu, with thicknesses around 1 to 3 nm [35].

A standard stack for this type of MR sensor consists of the following structure.

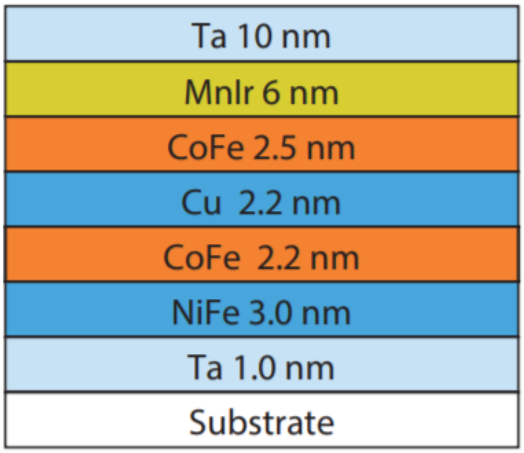


Figure 5 - Standard Spin-Valve stack illustration [35]

## 2.4 Linear MR sensors

The easiest way to measure the MR in an MR sensor is to measure the change in resistance plotted against an applied magnetic field. The junction area is inversely proportional to the junction resistance, given that the conductivity increases with the increase in electron conduction. Therefore, a resistance area product is introduced.

The demands of the signal response of the sensor may vary according to each specific application. For instance, for memory applications, such as MRAM, the response needs to have a square response, very hysteric and highly coercive, where the sensor is either in the parallel or antiparallel state. For sensing applications, we cannot have high coercivity. Instead, we are looking for a linear response. In this case, we have the free layer rotating coherently with an external magnetic field. At the same time, the sensor suffers a change in resistance until it reaches saturation, in the parallel or antiparallel state.

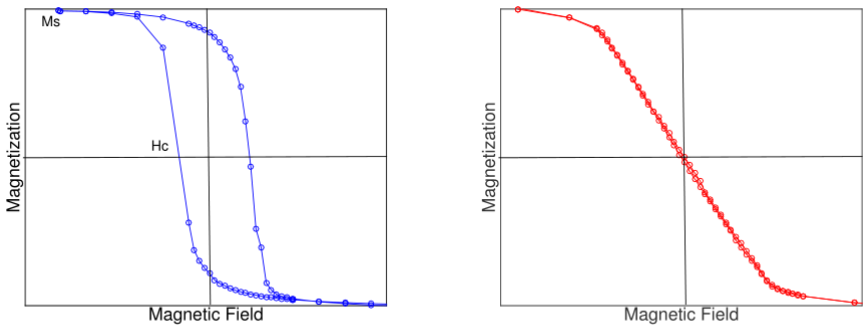


*Figure 6 - MR Curves according to two different intrinsic magnetic anisotropies, for the 1st, parallel like magnetizations, for the 2nd, perpendicular like magnetizations*

There are two possible configurations for an MTJ stack, parallel and crossed anisotropies. In parallel anisotropies, the easy axis of the pinned and reference layer are both magnetized in the same direction, while for crossed anisotropies, the magnetization of both layers is orthogonal.

To produce a squared transfer curve, both FM layers have to be magnetized parallelly to one another. This is conveniently achieved, because when depositing our FM material, our magnetic domains will normally align parallelly to one another.

To achieve sensor linearization, some techniques were studied and developed. For instance, at INESC-MN, the technique that is most regularly used is to take advantage of the self-demagnetizing field of the free layer when using a sensor geometry with high shape anisotropy [36]. This will lead to crossed anisotropies that is the most favorable magnetic conformation to produce a more sensitive device. But in order to achieve sensor linearization, this is not enough, the induced anisotropy term must be lower than the self-demagnetizing field of our device.

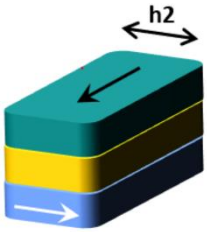


*Figure 8 - Magnetoresistance of a linear sensor according to parallel and antiparallel layers magnetizations*

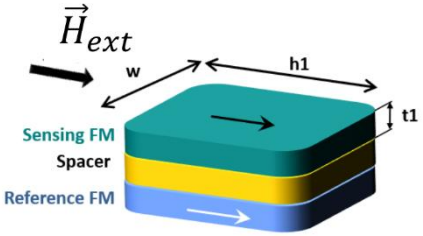


**Non linear**

*Figure 7 - Non-Linear MR response after the FM layer's deposition due to sensor stack configuration*

This method results in a MTJ with a linear response:

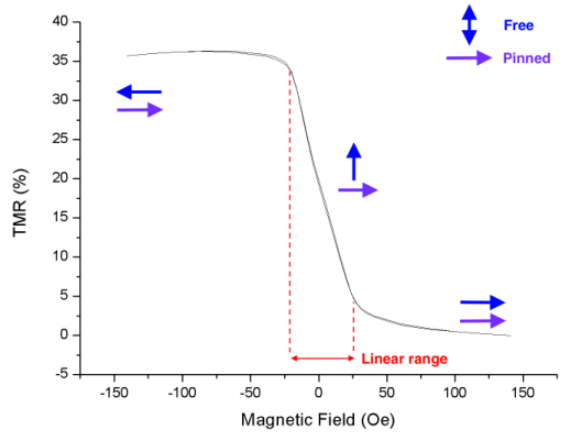


*Figure 9 - Magnetoresistance of a linear sensor according to parallel and antiparallel layers magnetizations*

## 2.5 Sensor Sensitivity

The sensor sensitivity is measured by the slope of the linear transition and is expressed by the following expression:

$$S\ sensor\ =\ MR\ /\ \Delta H\ [\%/Oe] \tag{7}$$

With ΔH being the magnetic field where he displays a linear response. A more significant slope will consist of a more sensitive sensor that will change its resistance value according to a minor variation of the external magnetic field.

## 2.6 Noise sources in MTJs and SVs

Noise exists in every passive or active electrical component and is manifested by voltage oscillations across circuit components. This signal should overcome the existing noise introduced by the sensor, electronic equipment, and surroundings to measure a robust magnetic signal. This creates the need to introduce an SNR, signal to noise ratio, to characterize the quality of our response signal.

In the case of MTJ's, there are two major noise contributors: electron tunnelling across the insulator barrier; magnetic fluctuations on the sensing layer. The primary noise sources are shot noise at nonzero bias voltages, thermal noise, 1/f noise from magnetic and electronic sources, and random telegraph noise [37].

### 2.6.1 Thermal Noise

Johnson-Nyquist noise, also known as thermal noise [38] [39], is a type of noise common in any electrical device. It is caused by a random thermal motion of electrons and is directly proportional to temperature, and is translated by the following expression:

$$Vth = \sqrt{4KbRT}\left[\frac{V}{\sqrt{Hz}}\right] \quad (8)$$

Here Kb is the Boltzmann constant, T is the absolute temperature, and R is the device resistance.

### 2.6.2 Shot Noise

Shot noise was introduced in 1918 by Walter Schottky. Shot noise is related to the current that flows through discontinuities in a circuit when all outside noise sources are removed. In MTJ's, the interface barrier presents a circuit discontinuity, where the electrons will tunnel through the barrier giving rise to small fluctuations in the current [36]. It can be described by the following expression:

$$\mathrm{Vshot} = \sqrt{2\mathrm{eIR}^2}\ [\mathrm{V}/\sqrt{Hz}\,] \quad (9)$$

Where e is the electron charge, I is the sensor's DC bias current, and R is the device resistance.

Shot noise is not very common on Spin-Valve structures.

### 2.6.3 Random Telegraph Noise

Oxygen vacancies in the tunnel barrier cause random telegraph noise in MTJ's. These vacancies can enclosure an electron, increasing the resistance of the device. When the system returns to the ground state, the electron is released, causing the system to decrease the resistance back to the original value. RTN increases with bias current and is usually predominant at low frequencies, however not always evident since it is shadowed by 1/f noise, which becomes dominant in the low-frequency regime [36].

### 2.6.4 1/f noise

This noise exists practically everywhere in nature and is usually related to charge trapping in crystal defects. There are two sources of 1/f noise, magnetic 1/f noise and electronic 1/f noise. Electronic 1/f noise is usually associated with charge trapping in interface barriers caused by defects in these barriers. As mentioned above, in RTN, this will lead to an increase in resistance. Nevertheless, oppositely to

RTN, the random liberation of this electron will follow a probability amplitude that favours energy concentration at low frequencies.

Consequently, the sensor intrinsic noise will be dominated by 1/f noise at low frequencies, critically limiting the sensor detectivity. The magnetic 1/f noise can be described by the magnetization switching of our FM layers at the interface between our free and pinned layers [40] [36]. This magnetic 1/f noise is also inversely proportional to the frequency. A frequency marks the threshold where the 1/f noise is lower than all other noise types; that is called the 1/f knee.

The expression that characterizes the 1/f noise is given by:

$$V_{1/2} = \sqrt{\frac{\alpha_H}{fA}} RI \ [\frac{V}{Hz}] \tag{10}$$

Where $\alpha_H$ is the Hooge parameter, f the frequency, A the area of the sensor, R the resistance of the device, and I the sensor DC bias current. The Hooge parameter can be separated into an electronic and magnetic contribution (varying according to the externally applied field), and it varies according to the concentration of electrical carrier, surface state density, and temperature:

$$\alpha_H = \alpha_{electric} + \alpha_{magnetic} \tag{11}$$

Hooge parameter increases with larger RxA and decreases with the bias voltage of the MR sensor [36]. The Hooge parameter is used as an indicator to compare the intrinsic noise level of each characterized sensor; a higher Hooge parameter means higher intrinsic noise.

## 2.7 Detectivity

Detectivity is defined by the slightest change in magnetic field that our sensor can detect for a particular frequency and applied field. This means that the sensor does not recognize any change below that value of magnetic field variation due to the total noise level overlap on our signal output.

Detectivity can be expressed by the output noise of the sensor divided by the sensor sensitivity.

$$D = \frac{S_V}{\Delta V \ / \ \Delta H} \ [\frac{T}{Hz^{\frac{1}{2}}}] \tag{12}$$

Where $S_V$ is the sensor's noise and $\Delta V \ / \ \Delta H$ the sensitivity.

To maximize detectivity, we need to minimize noise and maximize sensitivity, which translates into a TMR maximization for a minimum linear field range. Decreasing the Hooge parameter with, for instance, a decrease in our RxA parameter.

Another alternative to improve detectivity in MTJ's is to connect an array of MTJ in series. It has been proved that the detectivity decreases with increasing N by a factor of $\sqrt{}$ N [41], where N is the number of magnetic cells connected in the array.

## 2.8 Helmholtz Coils

The ability to produce arbitrary magnetic fields has always been a targeted ability ranging from magnetic resonance imaging to ambient magnetic field cancellation, hall sensors calibration, and magnetometer characterization. Some of these applications require a spatially uniform multiaxial magnetic field. To this end, the Helmholtz coil is a device that creates a highly uniform magnetic field consisting of two electromagnets on the same axis. A Helmholtz Coil consists of a paired arrangement of identical circular solenoids mounted coaxially at one coil radius from each other.

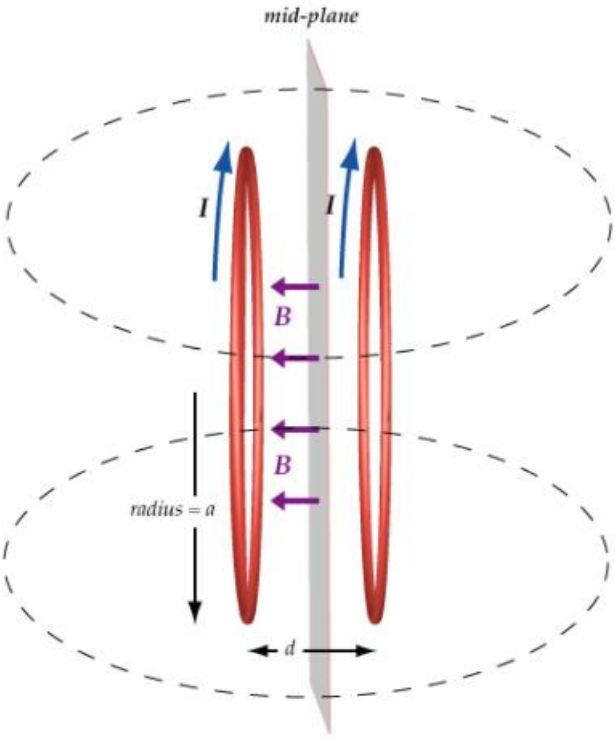


*Figure 10 - Helmholtz Coil exemplification and illustration*

To minimize the non-uniformity of the magnetic field generated, the coils separation distance is set to the coil's radius. At the center, the first three derivatives of the field strength with position all go to zero in every direction [42].

The derivation of the mathematical description for the magnetic field created inside the Helmholtz Coil begins with the formula that describes on-axis magnetic fields created by a single wire loop, that is itself, derived from Bio-Savart Law:

$$B_1(x) = \frac{\mu_0 I R^2}{2(R^2+x^2)^{\frac{3}{2}}} \tag{13}$$

Where R is the coil radius, I is the coil current, x is the coil distance on-axis, $\mu_0$ is the permeability constant. However, both coils contain several wire loops; the total current in the coil is given by,

$$\mathrm{nI} = \text{Total Current} \tag{14}$$

Where n is the number of turns in one coil. Substituting this in Eq. 4:

$$B = \frac{\mu_0 I R^2}{2(R^2+x^2)^{\frac{3}{2}}} \tag{15}$$

The geometric magnetic center is halfway between the two coils where x equals R/2, where R is the coil radius.

$$B = \frac{\mu_0 n I R^2}{2(R^2+(\frac{R}{2})^2)^{\frac{3}{2}}} \tag{16}$$

Per last, we have two identical coils, so we multiply equation 16 by two, hence deriving the following equation for the magnetic field generated in the center of the coils,

$$B = \left(\frac{4}{5}\right)^{3/2} \frac{\mu_0 n I}{R} \tag{17}$$

A 3D magnetic field can be created by integrating three orthogonal Helmholtz coils, each coil, defining one specific axis, X, Y, and Z, for a cartesian coordinate system. This system can generate a highly uniform magnetic field allowing magnetic field superimposition by different sets of coils.

### 2.8.1 Helmholtz Coils Uniformity

The uniformity of the magnetic field generated by the coils is an important parameter to consider if we want to construct an effective and efficient setup for magnetometer characterization.

One crucial factor for maximization of the field uniformity, as stated above, is the distance between the coils. When the coils are placed at a separation distance of the coil's radius, we maximize uniformity.

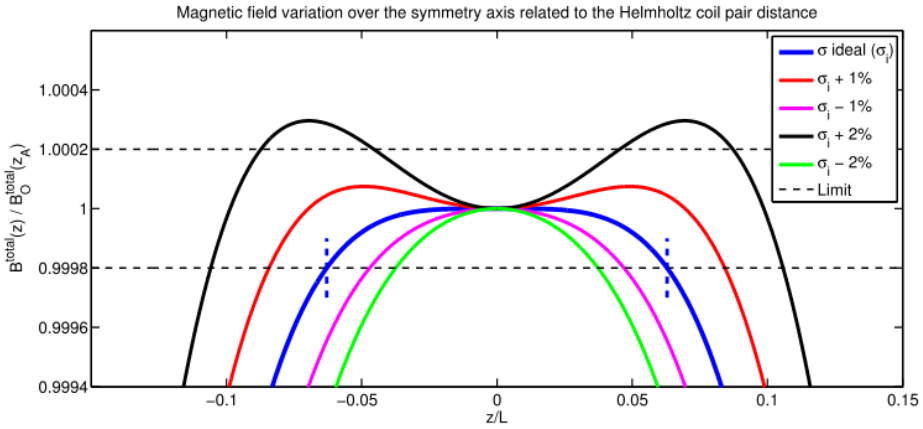

*Figure 11 - Magnetic Field uniformity variation over several Helmholtz Coil distance pairs, [43]*

Field variations for different distances between coils are used to determine the uniformity of the region according to the design requirements [43].

$$\beta = \left|\frac{\beta_{p(x,y,z)} - \beta_{central}}{\beta_{central}}\right| * 100\% \quad (18)$$

Where $\beta_{p(x,y,z)}$ is the measured magnetic field in a iven region of interest and $\beta_{central}$ is the measured magnetic field in the center of our device.

A second important factor is the number of turns and layers existing in a Helmholtz coil pair. It was observed that the field uniformity decreased with the increase in the number of turns per layer and increased with the increase in the number of layers [44].

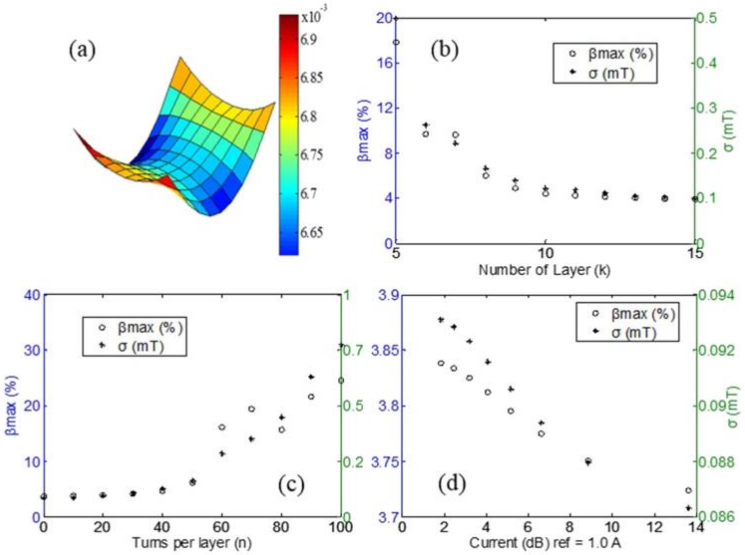


*Figure 12 - (a) magnetic flux density in the region of interest; uniformity variations with the changes in (b) the number of layers, (c) turns per layer and (d) operating current [43]*

The field uniformity can be substantially improved when we increase the number of layers combined with a decrease in the number of turns per layer. The Setup should be designed to fulfill these characteristics, noting that the operating current should not be too large, which aligns with the requirements of coil-heating.

This is translated with a smoother transition curve when considering the field uniformity for thin winding coils (more turns, fewer layers) versus thick winding coils (fewer turns, more layers).

# Chapter 3

## Experimental Techniques

### 3.1 Magnetotransport Characterization Techniques

To characterize our MTJ sensors, we used a manual prober setup, also known as 140 Oe setup.

#### 3.1.1 140 Oe Setup

This Setup consists of a Helmholtz coil powered by a current supplier, a bipolar operational amplifier (Kepco BOP BIT488.2), which creates a magnetic field from -140 to 140 Oe. The MTJ is placed at the geometric center of the Helmholtz coil, where field uniformity is maximum. To measure the change in resistance of our sensor, we use a two-probe setup, consisting of two tungsten probes, with a special resolution of 10um, that we place on top of our MTJ contacts. The probes apply a constant electrical current and measure the output voltage at its terminals. To measure the output voltage and supply our constant electrical current, we used a current source (Keithley 220) and a Sensitive Voltage Reader. In addition, the positioning of the probes is done manually with the help of an optical microscope to allow the proper positioning of our needle's probes.

This is all connected to the GPIB that communicates directly with the software that automatically collects the required data and establishes a MR curve for the given sensor.

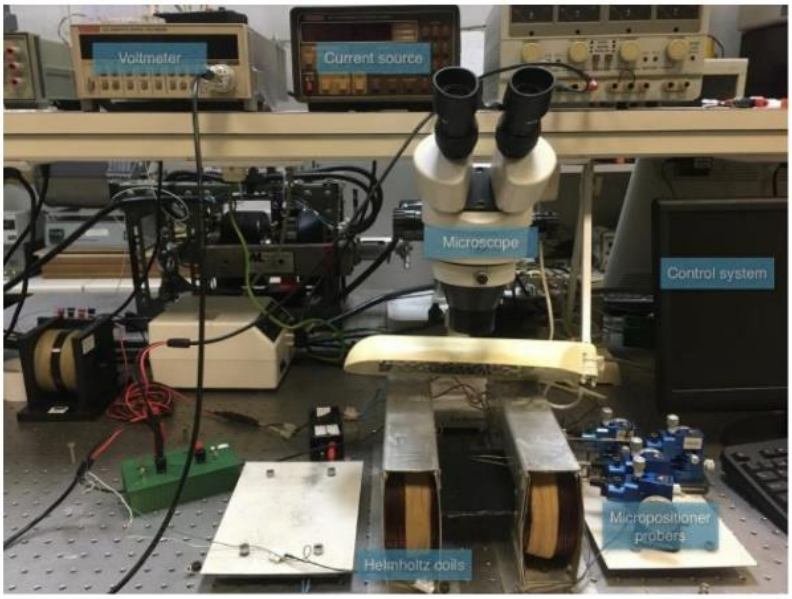


*Figure 13 - 140 Oe Setup*

## 3.2 Noise Measurements

The noise measurements are the last stage of sensor characterization. To measure the sensor's noise, no magnetic field is applied, done at zero Tesla field.

Two shielded boxes constitute the noise setup. The first box is a circuit composed of two potentiometers that regulate the current that crosses our sensors terminals, providing us with a Rpotentiometer varying from 0 to 20 or 100 KOhm. The input voltage comes from a 1.5 V battery. The Rpotentiometer is then regulated to provide our sensor with our desired Vbias, calculated from the formula below.

$$\mathrm{Rpo} = (\mathrm{Vbias}/\mathrm{Vbat} - 1) * \mathrm{Rdut} \quad (18)$$

Where Rpo is the resistance o our potentiometer, Vbias is the bias voltage introduced into our sensor and Rdut is the resistance of our sensor.

The output from our primary shielded box goes directly into an amplifier (SIM919 JFET). The amplifier is supplied by a pair of 10 batteries of 1.5 V each. The gain is adjustable from 1 to 500, being the value used in every measurement in our noise setup, 100 (40 dB). This gain translates into a constant noise level of 4nV/√(Hz).

Two data acquisitions must be obtained for complete noise measurement, one with applied current and another without it. Two measurements were made in the 0-1Khz range and two others more in the 0 - 100Khz range. The RBW from each set of data is 2 and 200 Hz, which gives a smaller frequency span with better sampling resolution for the 1st data acquisition and a wider frequency span with worse sampling resolution for the 2nd data acquisition.

The measurement without current acts like a calibration curve that eliminates the sensor's noise related to all other circuit components besides the sensor, essentially, thermal noise.

## 3.3 Helmholtz Coil Characterization Techniques

The Bipolar Operational Amplifier was used to supply several current steps to generate a proportional magnetic field to proceed to the 3D Helmholtz Coil characterization. A hall probe sensor magnetometer was positioned at the exact geometric center of the respective Helmholtz coil being calibrated to measure the magnetic field generated, individually, for each one of our Helmholtz coils.

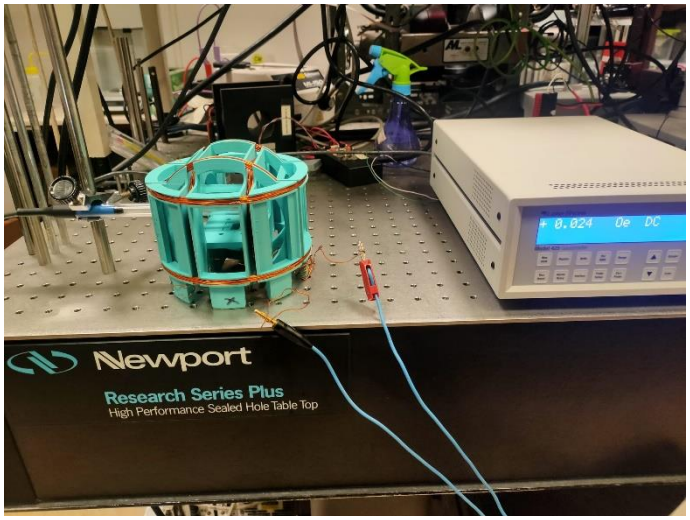


*Figure 14 - 3D Coil Setup calibration*

Finally, to measure the established uniformity for each coil, we shifted the hall sensor magnetometer, with a constant generated magnetic field, to measure the change in the magnetic field over the given axis.

# Chapter 4

## Helmholtz Coil Fabrication

### 4.1 Simulation Process

#### 4.1.1 Simulator

To design the respective Helmholtz coil, an open-source python library was used, magpylib. This python library is used for calculating magnetic fields, currents and provides the necessary tools to generate, manipulate and visualize assemblies of magnetic sources.

Using this library, a script was developed on an integrated development environment called spyder to calculate the necessary coil parameters to obtain the desired requirements for our Setup.

One of these requirements consists of holding inside the Setup a sensor with a maximum size of 5x5 $cm^2$. This Setup was created to generate very small magnetic fields to characterize MTJ with different conformations and structures to create a minimal low-frequency field. Moreover, specific parameters must be established, such as the minimum detectable field, fixed at 1pT, translating to around 1 nA of induced current into our coils. In addition, we defined the cooper wire diameter at 0.8 mm and introduced it in our input parameters.

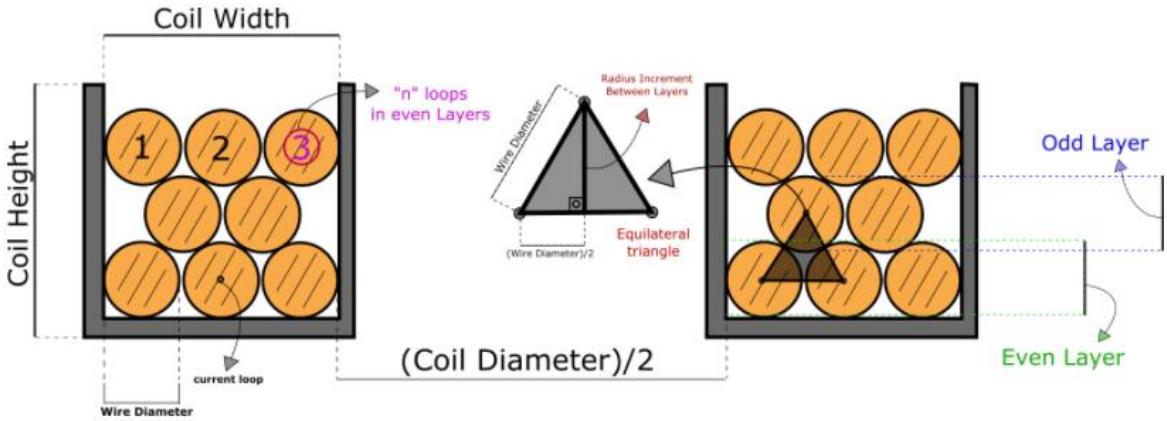


*Figure 15 - Helmholtz Coil Cross Section*

This cross-cut section shows several parameters that need to be defined as the “even” and the “odd” layers while considering the number of loops in each of these layers. Three more parameters were then initialized, the number of even, odd layers and the number of turns per even layer.

The input parameters and the console output are presented in the attachments.

Output parameters are the coils specific design, dimensions, wire dimensions, and power dissipation in each coil axis.

### 4.1.2 Graphical Results

Some graphical results were constructed for each axis to understand better the difference in magnetic field uniformity that specific parameters can enhance. For each axis, the simulator plotted the magnetic field amplitude for a given region of interest, the field uniformity, and a 3D graphic display of how the system will look.

After several simulations, we enhanced homogeneity for the input parameters shown above with the following graphical representation.

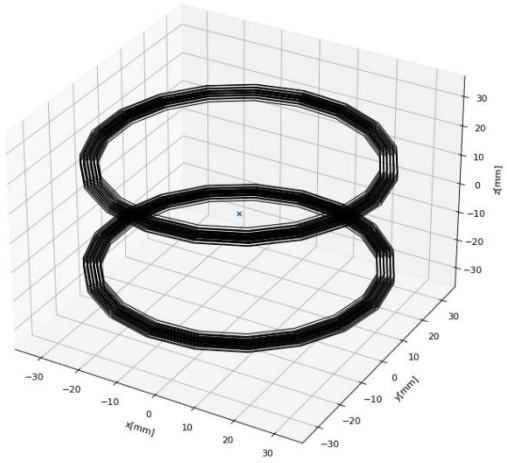


*Figure 16 - Z-Axis Graphical Representation*

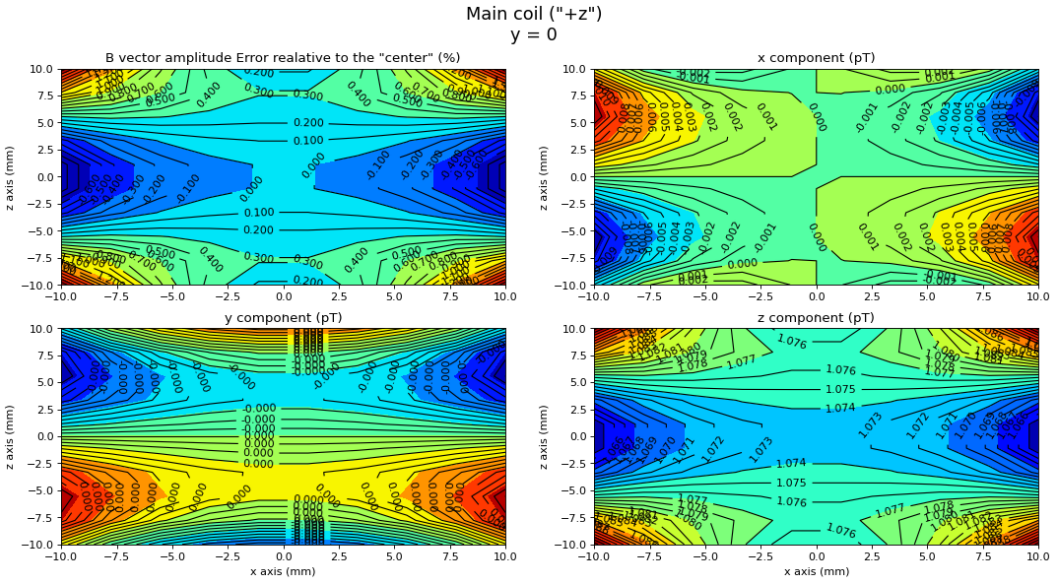


*Figure 17 - Z-Axis Uniformity Simulation*

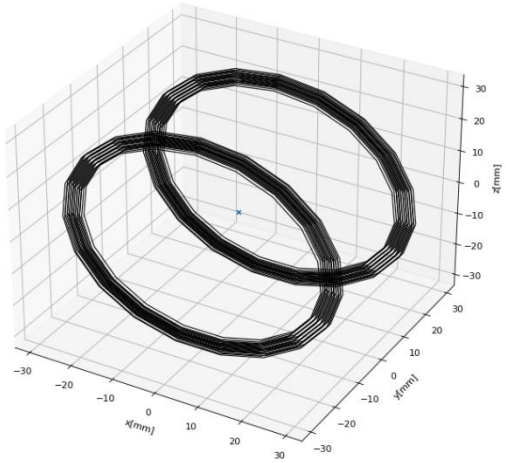


*Figure 18 - Y-Axis Graphical Representation*

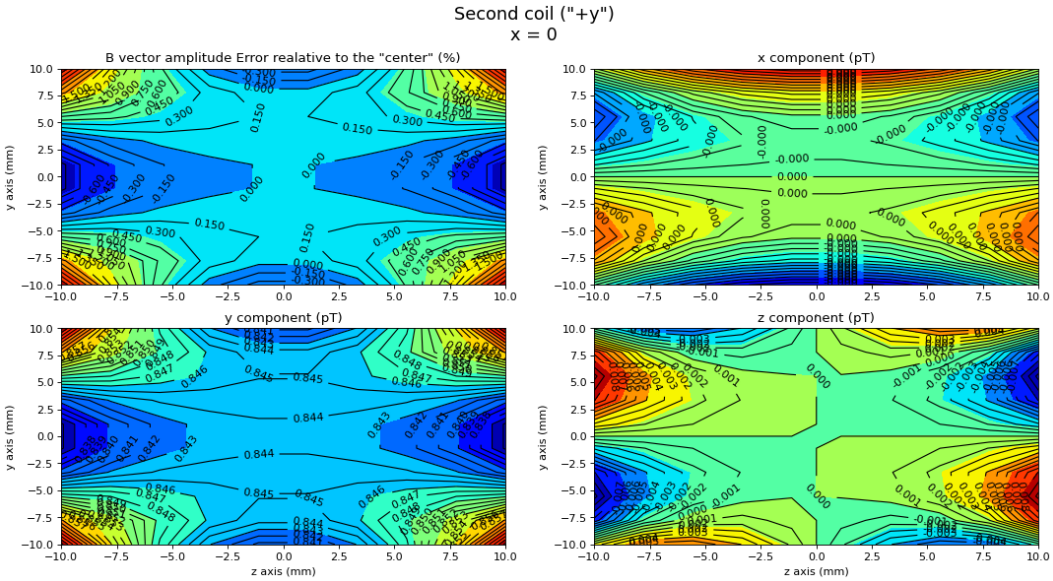


*Figure 19 - Y-Axis Uniformity Simulation*

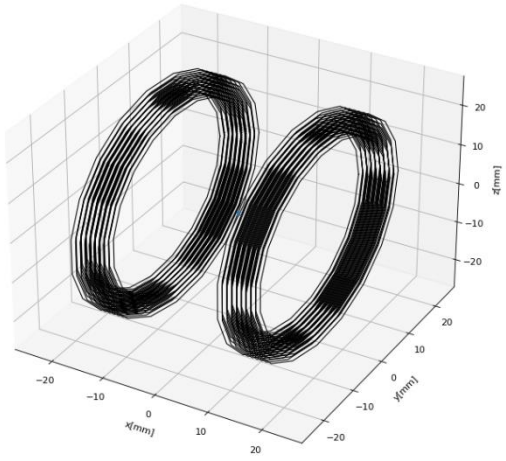


*Figure 20 - X-Axis Graphical Representation*

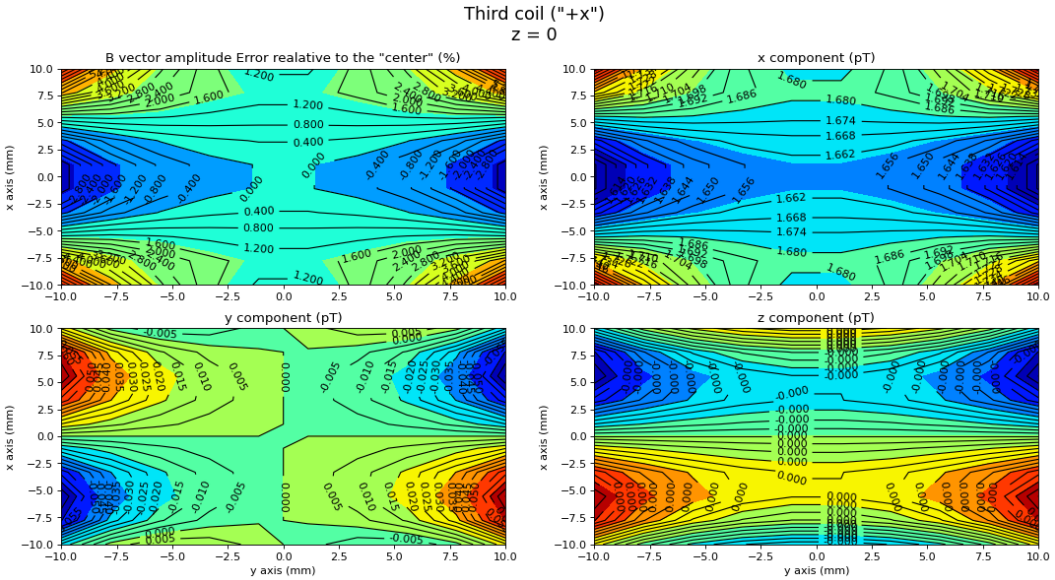


*Figure 21 - X-Axis Uniformity Simulation*

As mentioned above, the field uniformity presents a considerable dependence on these parameters, which should not be chosen arbitrarily.

### 4.1.3 Simulator Results

The parameters used to construct the coil are shown in the following table.

*Table 1 - Helmholtz Coil Parameters*

| Coils | Radius (cm) | Coil Height (cm) | Coil Width (cm) | Length of Wire (m) | Wire Diameter (mm) | Nº Turns |
|---|---|---|---|---|---|---|
| X-axis | 42,5 | 6.6 | 9.65 | 6 | 0.8 | 46 |
| Y-axis | 56,15 | 4 | 5.5 | 3.7 | 0.8 | 21 |
| Z-axis | 66,5 | 4.65 | 5.5 | 5.64 | 0.8 | 27 |

### 4.1.4 Coils Parameters

*Table 2 - Resistance, Current and Voltage for 1uT Magnetic Field Induction*

| | Resistance (Ohm) | Current (mA) | Voltage (mV) |
|---|---|---|---|
| X-Coil | 0.84 | 1.03 | 0.863 |
| Y-Coil | 0.51 | 2.97 | 1.51 |
| Z-Coil | 0.77 | 2.74 | 2.11 |

*Table 3 - Resistance, Current and Voltage for 1uT Magnetic Field Induction*

| | Resistance (Ohm) | Current (nA) | Voltage (nV) |
|---|---|---|---|
| X-Coil | 0.84 | 1.03 | 0.86 |
| Y-Coil | 0.51 | 2.97 | 0.15 |
| Z-Coil | 0.77 | 2.74 | 0.21 |

## 4.2 Fabrication Process

To fabricate the model, a 3D modeling software named SolidWorks was used. The geometric model of our 3D Helmholtz Coil is based on the previously obtained parameters by our simulator. The model was designed to align our coils in each specific axis perfectly, which led to the assembling of every coil integrated into a single modeling part.

This was later exported, saved, and introduced into the software of the INESC-MN 3D printer, which printed the device using PVA. Here follows the result of the coil setup:

Followed by Coil Winding

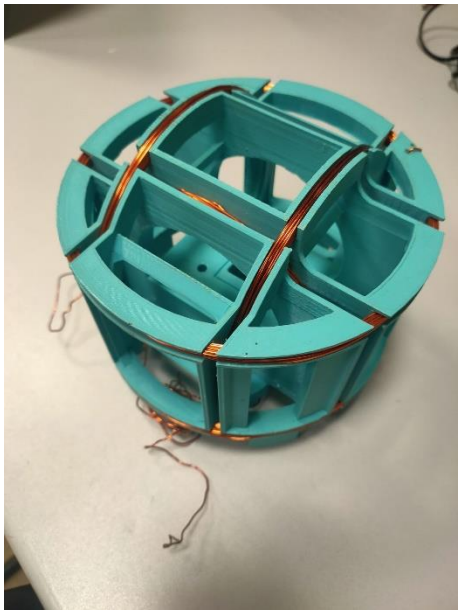

*Figure 22 - 3D Coil Setup Final Device*

## 4.3 Coils Calibration

Proceeding to setup calibration, a bipolar operational amplifier called kepco bop bib488.2 was used to supply current to the 140 Oe setup and, consequently, to power this Setup. In addition, we used a gaussmeter to measure the magnetic field generated in the geometric center of our coil. This yielded three calibration curves that were matched against the magnetic field theoretical values calculated for each current input. The data was collected manually, such as coils input current from a multimeter connected in series with our current source and the magnetic field directly from our gaussmeter.

Here follows the retrieved data from the magnetometer calibration:

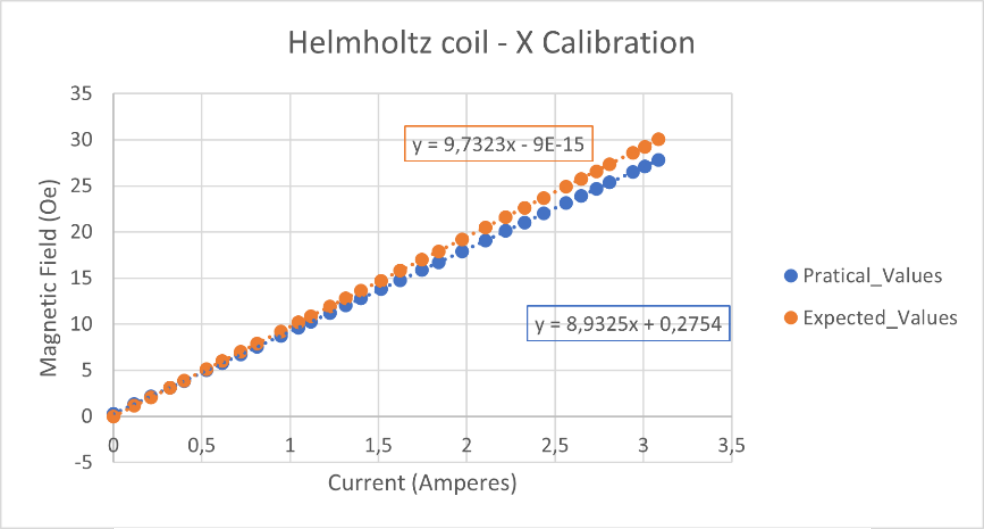


*Figure 24 - Helmholtz Coil X Calibration*

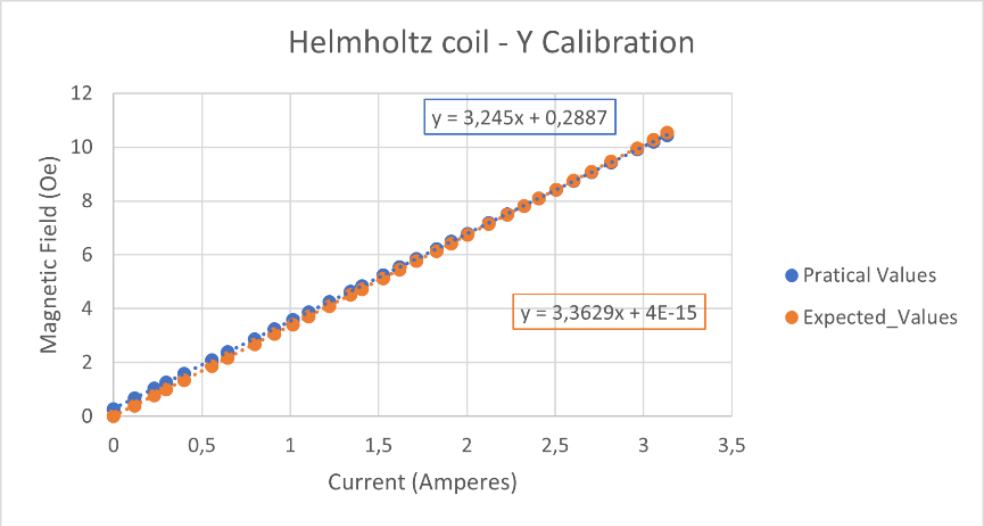


*Figure 23 - Helmholtz Coil Y Calibration*

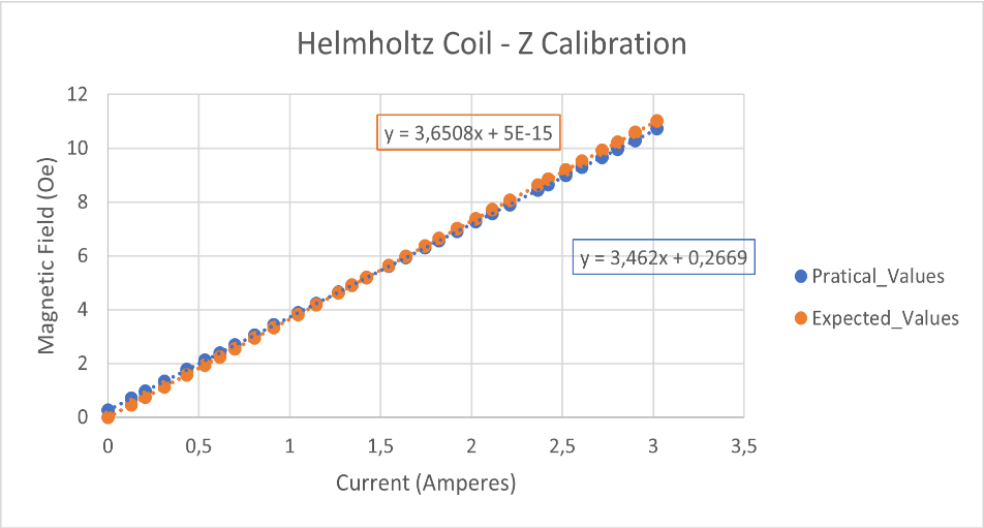


*Figure 25 - Helmholtz Coil Z Calibration*

The slope difference between the calculated and experimental values is most likely due to the magnetization of surrounding metals. Also, the theoretical values did not took into account the earth's magnetic field.

# Chapter 5

## Assembly of MR Sensors

### 5.1 Chip Carrier

Since size was one of the primary focuses, the chip carrier we chose needed to be large enough to allow sensor manipulation but small enough to possess a particular competitive advantage. The chip carrier chosen was a Quad Flat No Leads (QFN), of 6x6 $mm^2$, with electrical connections on the bottom of the carrier. To establish the contacts in our carriers, we needed a solution that could allow the facile replacement of the carrier by another carrier with different sensors since this work aims to allow the characterization of several low field sensors. To this end, we coupled our carrier with an open-top socket to acquire the sensor's signal where the carrier could be easily removed and substituted by another.

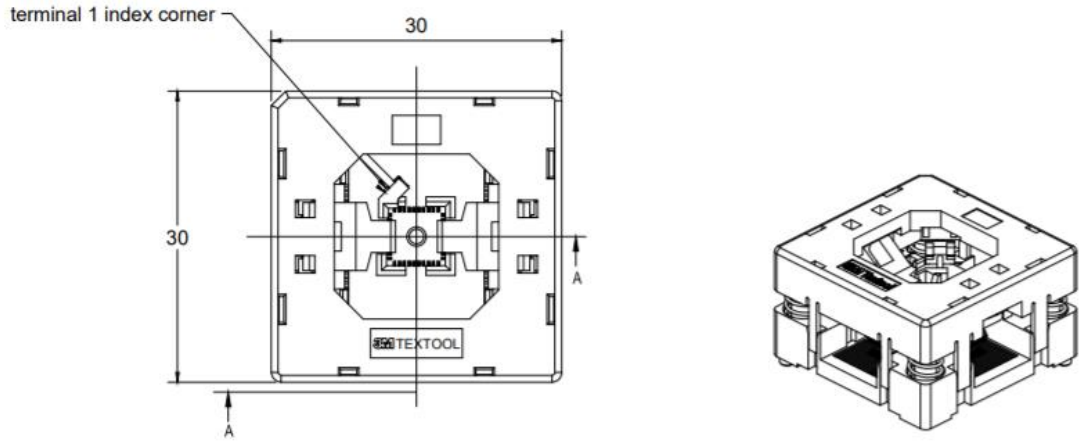


*Figure 26 - Socket model illustration and diagram*

Meanwhile, a PCB (5x5cm) was designed to establish the breakout from the socket to 4 arrays of 10 pins on each side of our PCB.

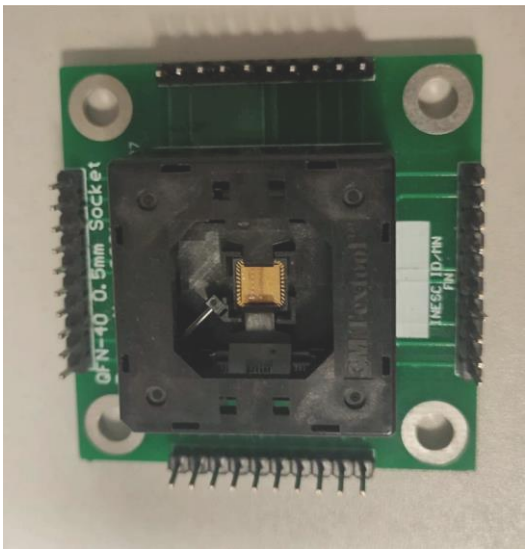


*Figure 27 - Final assembled device, socket + PCB + Sensor*

## 5.2 Sensor Assembly

Several specific sensors were assembled to understand how reliable and prone the 3D Coil setup regarding sensor characterization is.

### 5.2.1 3D Magnetometer from array of Magnetic Tunnel Junctions of AlOx

In this work, we used several arrays of MTJ sensors prevenient from a Master Thesis elaborated by Mafalda Vieira Garcia de Oliveira, where she microfabricated a 6-inch wafer of AlOx MTJs, where each sensor is 1x1.5 $mm^2$. Here follows the description of the MTJ stack:

**Buffer** Ta and Ru alternate layers were used. Despite the Ta layer having a big resistivity (154μΩ.cm), it compensates by lowering the resistivity of the FM layers. In addition, to balance the high resistivity of the Ta layer, we used a Ru layer, which possesses a smaller resistivity (10μΩ.cm) and lowers the total resistivity of the buffer layer.

**Free Layer** CoFeB FM layers were used by presenting the best spin polarization, therefore enhancing our TMR ratio. NiFe was also used as part of the free layer electrode to improve the magnetization reversal properties.

**Insulating Layer** Al2O3 spacer was used

**Pinned and Reference Layer** Synthetic Antiferromagnetic structures are constituted by two FM layers separated by a non-magnetic spacer. The two FM layers are CoFeB, the reference layer, and the pinned layer, NiFe. The spacer is Ru, with 6 A of thickness, maximizing the antiferromagnetic coupling between the two layers. The antiferromagnet used to pin the magnetization direction of our pinned layer is MnIr.

**Cap Layer** The cap layer is composed of two layers of Ru and Ta.

Exemplificative stack diagram of our MTJ:

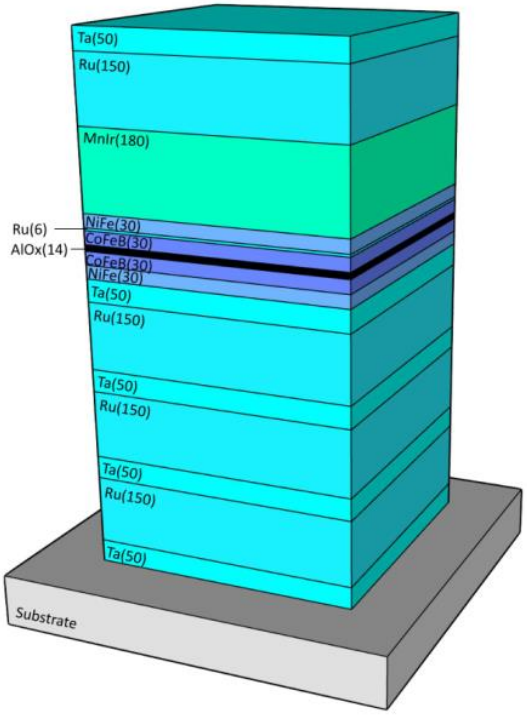


*Figure 28 - Stack illustration of Mafalda Veiga Thesis MTJ's [33]*

Ultimately, the final goal of this sensor is based on the ability to measure 3D magnetic fields while maintaining a compact size device. Therefore, this would require some planning regarding the disposition of the sensor. One of the possibilities was incorporating a vertical PCB with our array of MTJ's to define our Z-axis. On the other hand, this would not be a very compact solution. Since the vertical PCB was not an option, we tried to integrate the MTJ array vertically, right on top of the chip carrier.

This attempt to rotate our sensor ninety degrees in the longitudinal axis was time-consuming because it required a wire bounding in two orthogonal planes instead of just one, which is the case of regular wire bonding. The wire bonding machine existing at INESC does not rotate the stage out-of-plane, which means that to proceed to the wire bonding, the sensor would need to be rotated after the wire bound on the sensor contact pads. This is a tricky maneuver to attempt without breaking the wire. In addition, the pads were passivated with Ta, which with the wire material and needle size, difficulted the attachment of the wire to the contacts.

This maneuver took place in three different scenarios.

The first scenario was to attempt the regular wire bonding with the sensor in the horizontal position, as for the X and Y directions, and then rotate and glue the sensor without breaking the wire.

The second scenario was to glue our sensor to a flexible cable leading to two-wire bonding instead of only one. The first step was to cut the flexible cable and bend it into an L format. The second step would be to glue the sensor into the flexible cable and establish the wire-bound between the sensor and the flexible cable in the same plane. Then we would rotate the flexible cable, glue it to the chip carrier and proceed to the wire bounding from the flexible cable to the sensor, again in the same plane.

The third scenario was to wire bound the sensor pads, with the sensor horizontally placed on top of our carrier, and leave a certain amount of loose wire, not establishing the second bound on the chip carrier. Then, very carefully, rotating and gluing the sensor to afterward push the loose end of the wire into the chip carrier contacts, establishing then the second bounding.

The more prominent maneuver was the third option; the first, due to high tension between the wire, the rotation was practically impossible. Unfortunately, for the second scenario, the flexible cable did a cushion effect when the wire bonding took place, absorbing some energy placed into the bounding, resulting in no wire attachment.

In conclusion, a successful 3D magnetic sensing device was able to be fabricated with this vertical build.

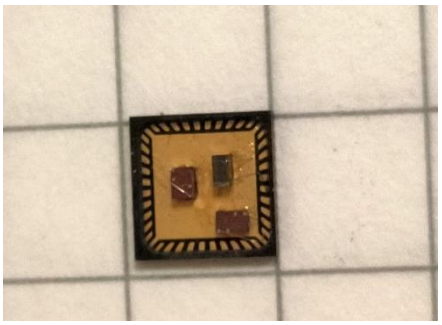

*Figure 29 - 3D Magnetometer*
*Final assembled device*

### 5.2.2 Two MTJ's sensors provided by INESC-MN

Two types of TMR sensors were provided by INESC-MN, from one of the Multiproject Wafer run (MPW run #11) from a 200mm diameter wafer. The chip sizes are (0.68x0.40$mm^2$) and (0.30x0.42$mm^2$), which includes TMR sensors which consist of a series of 96 pillars, each pillar with 8 um diameter size. The stack was deposited on a Si/SiO2 200nm wafer and consists of:

Si/SiO2//[Ta5/Ru10]x3/Ta5/Ru 5/MnIr 8/CoFe 2.2/Ru 0.75/ CoFeB 2/ MgO 1.55/CoFeB 1.6/Ru5/Ta 5/TiWN 30 (thickness in nm).

For readability purposes we will call them respectively, MTJ 1 and MTJ 2, for the (680 um x 400um) chip and the (300um x 420um) chip.

The incorporation of these sensors into our chip carrier was done by normal wire-bounding onto our QFN.

### 5.2.3 Spin-Valve with and without Flux concentrator

For last, two spin-valves sensors were used with the same characteristics except for, in one of the sensors, the incorporation of a flux concentrator in the silicon substrate. The flux concentrator objective in this sensor is to deviate the magnetic flux lines of other sensitive directions into the sensor's sensible direction. These sensors were built and characterized to determine the main noticeable differences between both sensors' sensitivity, detectivity, coercivity, and linear response. Each sensor has a size of 1.7x0.65 $mm^2$and 1.95x1.65 $mm^2$, for Spin-Valve without and with Flux-Concentrator.

The corresponding Spin-Valve is the following:

Glass/Ta 5 /Ni81Fe19 2.5/Co80Fe20 2.8/Cu 2.4/Co80Fe20 2.4/Mn74Ir26 7/Ta 5, (thickness in nm).

The incorporation of these sensors into our chip carrier was done by normal wire-bounding onto our QFN.

## 5.3 Sensor MR Curve

### 5.3.1 Acquisition Software and Electronics

To acquire the MR curve from our 3D sensor, the 3D Helmholtz coil was used. To that end, a script was elaborated in Visual Studio under the programming language C#.

Intending to create a changing DC magnetic field, the 3D coils setup was fed with several constant steps of DC current programmed by our script. Unfortunately, the power supply could not provide the demanded steps of current to the Setup. The bipolar operational amplifiers rapidly grew into a voltage limit situation which disabled us from obtaining a steady and constant magnetic field window. Instead, we manually increased and decreased the current in a continuous mode while the data was collected with a fixed timestamp equal to half a second.

The script used the calibration curves for each Helmholtz Coil axis to transform every current input received by our coils into the respective value of the applied magnetic field. Meanwhile, we collected the voltage at the sensor terminals using a two-probe method, which applies a constant current, Ibias,

in the outer sensor’s contacts while measuring the voltage simultaneously. By using Ohm’s law, V = RI, we can easily calculate the sensor’s resistance, hence, plotting our MR curve.

All the devices, as for, Voltmeter and both current sources, Coils, and Ibias, were all connected to GPIB that for himself, connects to the computer, where the proper software was installed to be able to run the C# script on Visual Studio.

The input parameters are the desired axis in the 3D coil setup, the desired number of measurements, and the interval between them.

The C# code script is presented in the attachments.

# Chapter 6

## Sensor's Characterization

### 6.1 MR Curve Characterization

For every sensor characterized in this project with the 3D Coil Setup, another characterization was done with the 140 Oe setup to observe the possible disparity between the commonly used Setup at INESC-MN to calculate MR curves and our own built 3D Coil Setup.

#### 6.1.1 MR Curve for our 3D Magnetometer

The sensor was successfully characterized regarding his MR curve. As the linear range presented by our 3D Magnetometer sensors is in the order of -50, 50 Oe, the entire linear range could not be characterized through the 3D coils setup due to the coil's small size, leading to a considerable power dissipation for currents above 3.5 Amperes.

The linear range was partially represented in the following MR plots for the three spatial axes for our 3D Coil Setup and 140 Oe Setup. A linear tendency line was calculated for every plot to make a more fitting comparison between the two setups.

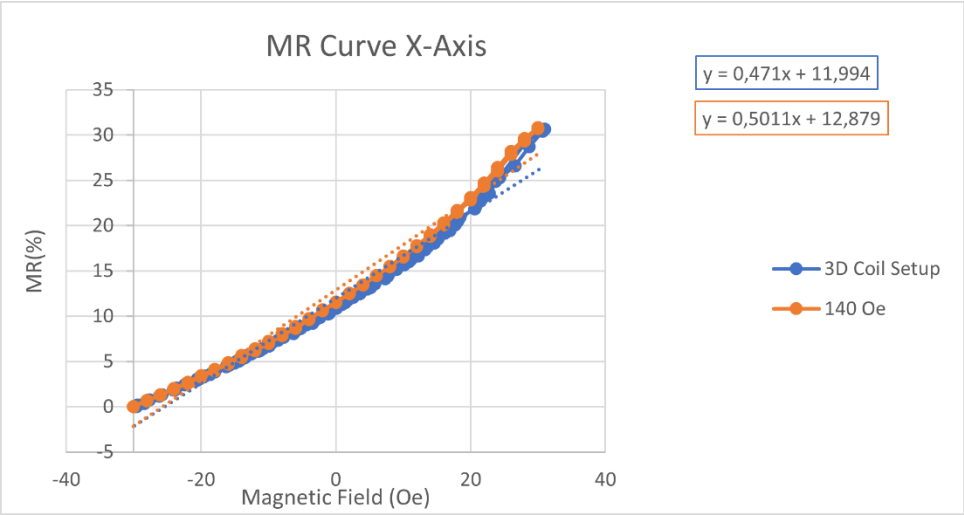


*Figure 30 - Linear range of magnetoresistive curve for the X-Axis*

We can see a very close similarity between the slope of both our linear tendency lines for the X-axis. We can plot our MR curve ranging from approximately -25 Oe to 25 Oe in the X-axis, corresponding to 50% of the entire linear range.

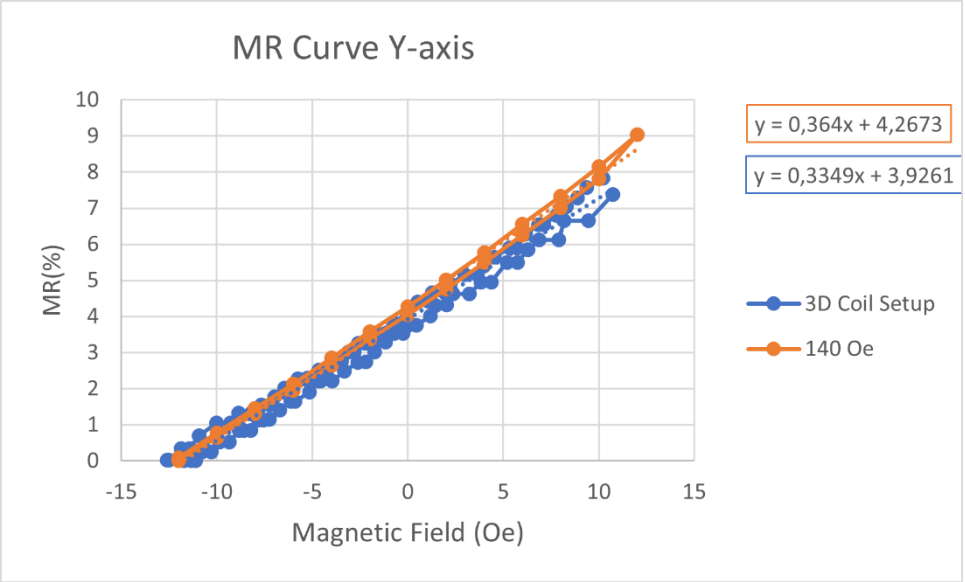


*Figure 31 - Linear range of magnetoresistive curve for the Y-Axis*

We can also see a close similarity between the slope of our linear tendency's lines for the Y-axis. However, the coercivity between both setups varies more in the X-axis. We can plot our MR curve ranging from approximately -10 Oe to 10 Oe, corresponding to 20% of the entire linear range.

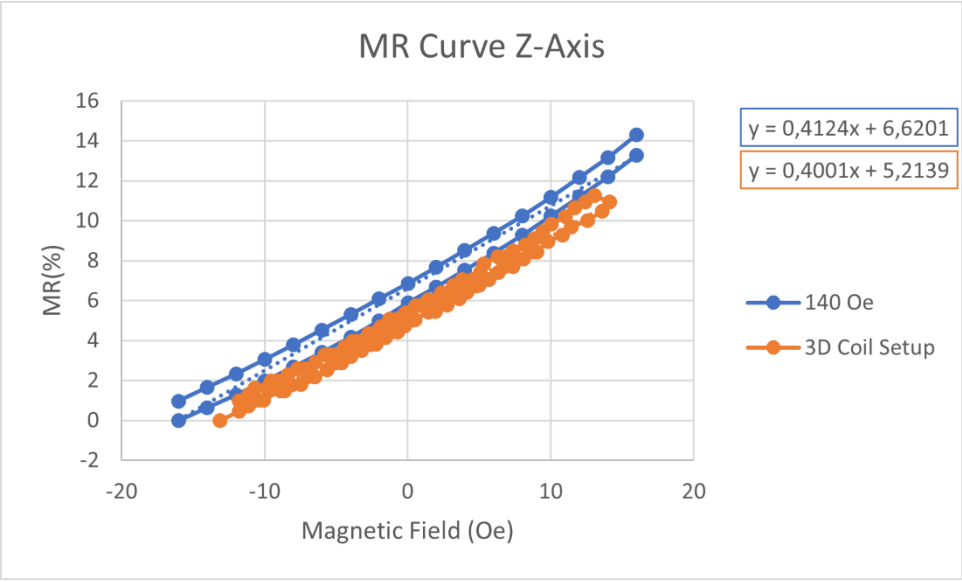


*Figure 32 - Linear range of magnetoresistive curve for the Z-Axis*

We have the most similar slope sensitivity of our MR curves for the Z-axis. However, the coercivity is still very different, and the disparity between MR values is more significant. One of the possible explanations for this could be the fact that the Z sensitive direction was hard to achieve in the 140 Oe,

since it had to be placed orthogonally to the usual chip carrier disposition, without having a built a flat surface to allow a perfectly flat and Z-axis coincident surface. We can plot our MR curve ranging from approximately -10 Oe to 10 Oe in the Z-axis, corresponding to 20% of the entire linear range.

From the given plots, we can notice a close similarity between the tendency line from the linear range MR curves of both setups. By comparing for each direction, the slopes of the linear sensing area, we get a 6% (X-Axis), 8% (Y-Axis), and 3% (Z-Axis) difference from the reference values of the 140 Oe setup.

The obtained difference is believed to be led by geometrical imprecision, which could be improved if we build another structure integrated into the 3D Coil Setup that would lock the chip carrier in the geometrical center of the coils. One other possible explanation could be the number of voltages reading averages measures of our sensor by the 140 Oe Setup. In our script, the voltage was directly read from the voltmeter, without measured averages, leading to some data disparity.

### 6.1.2 MR Curve for MTJ 1 and MTJ 2

The sensors were successfully characterized regarding their MR curve.

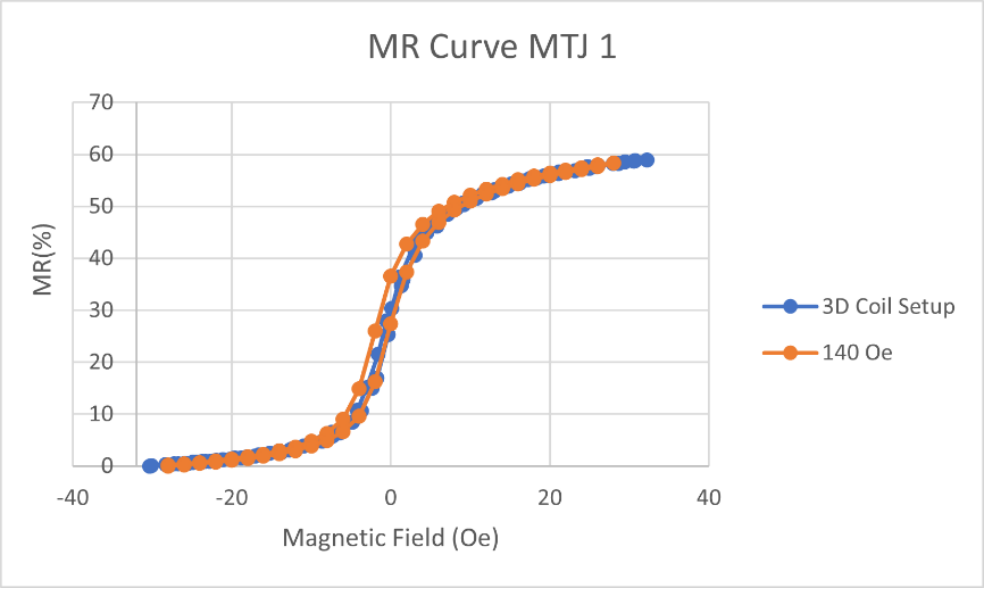


*Figure 33 - Magnetoresistive curve characterization of MTJ 1*

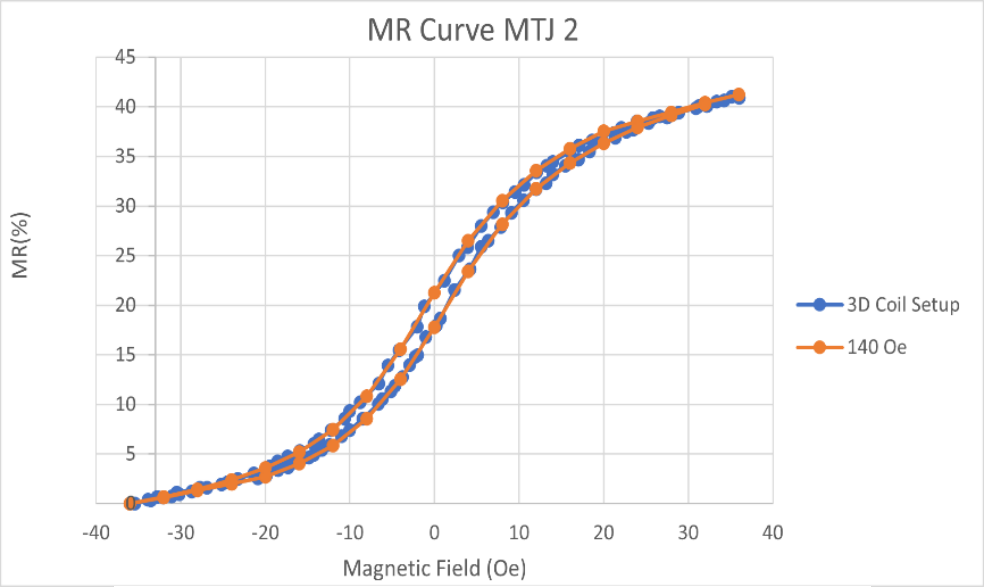


*Figure 34 - Magnetoresistive curve characterization of MTJ 2*

Table 4 - MR specific data for MTJ 1 and MTJ 2

| | Sensor | Ibias (uA) | Ro (KOhm) | MR (%) | Sensitivity (mV/Oe) | Coercivity (Oe) |
|---|---|---|---|---|---|---|
| 140 Oe | MTJ 2 | 1 | 556 | 41.24 | 16.59 | 2.55 |
| | MTJ 1 | 1 | 354 | 58.3 | 25.57 | 2.00 |
| 3D Coil Setup | MTJ 2 | 1 | 555 | 40.91 | 16.56 | 2.58 |
| | MTJ 1 | 1 | 350 | 58.87 | 28.68 | 0.38 |

Both sensors present a very similar behavior in our measured setups, presenting a percentual MR difference of 1% for MTJ 1 and MTJ 2.

### 6.1.3 MR Curve for Spin-Valve sensors

MR spin-valves are often coupled with flux concentrators because their magnetic flux increases through the Spin-Valve sensing direction. This will theoretically lead to an increase in the sensitivity of our sensor if the magnetic flux is correctly shifted.

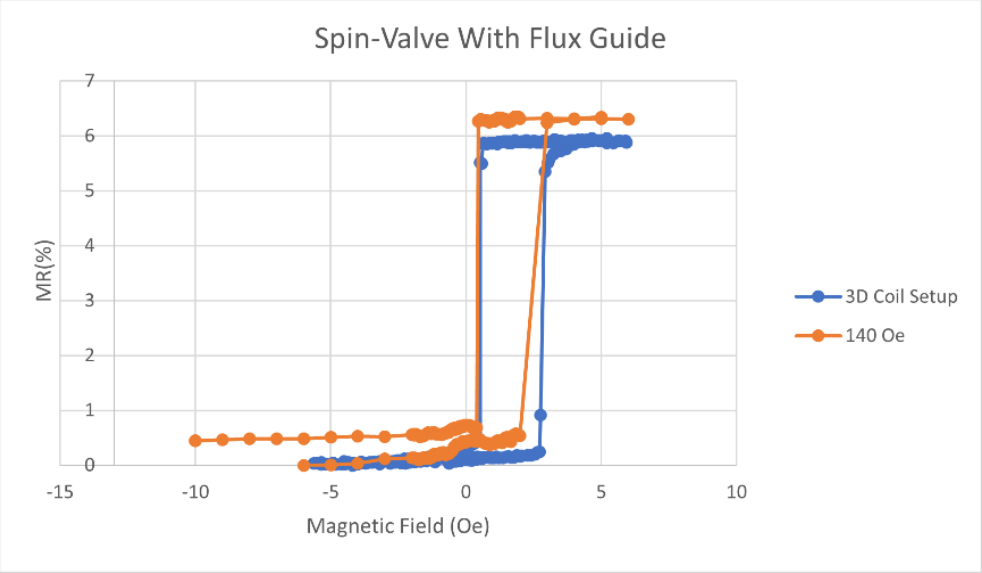


*Figure 36 - Magnetoresistive Curve for Spin-Valve with Flux Guide*

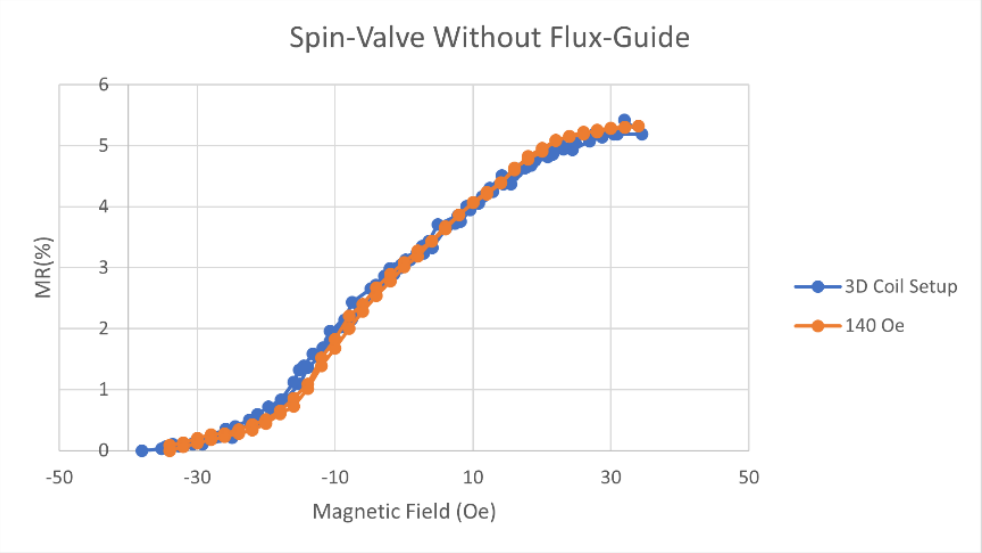


*Figure 35 - Magnetoresistive Curve for Spin-Valve without Flux Guide*

Below is a table that will summarize the results obtained in the previous MR curves.

*Table 5 - MR specific data for Spin-Valve with and without flux-guide*

| | Sensor | Ibias (uA) | Ro (kohm) | MR (%) | Sensitivity (uV/Oe) | Coercivity (Oe) |
|---|---|---|---|---|---|---|
| 140 Oe | Flux | 1 | 17.53 | 6.30 | 162 | 1,7 |
| | N/ Flux | 1 | 18.66 | 5.32 | 0.39 | 0.2 |
| 3D Coil Setup | Flux | 1 | 16.54 | 5.89 | 134 | 2.35 |
| | N/ Flux | 1 | 18.15 | 5.19 | 0.36 | 0.35 |

Both sensors present a very similar behavior in our measured setups, presenting a TMR difference for our Flux concentrator and No Flux concentrator sensor of 6.5% and 2.4%, respectively. The sensitivity was still slightly different for our flux concentrator sensor, almost doubling the value. This was consistent throughout several measurements done in this and other similar sensors. The stepper and more sensitive response in the 3D Coil Setup was linked to how the measurement was done in the 140 Oe setup, with a more significant magnetic field disparity between the points in the critical sensing area. This could have been avoided with a measurement that would consist of a smaller interval between the induced magnetic field in the coils and the correspondent voltage measurement. One possible solution could also be a more significant amount of measured voltage points in the linear sensor range.

As expected, we see an increase in the sensitivity of our sensor of about 400 times the value of our spin-valve without the flux concentrator. Despite this increase in sensitivity, we have more coercivity, which cannot always be beneficial depending on the circumstances.

In general, the MR curve for both sensors measured in two different setups was very approximated with some room for improvement, such as, the precise geometrical alignment of the sensor in both correspondent setups.

Despite the encountered difference, we can infer the proper functionality of our 3D sensor and our 3D Coil setup.

## 6.2 Sensor Noise Measurement

To measure the noise curve for the existent sensors, we used the Noise Setup existing at INESC-MN and used a conversion software to interpret the data. All the measurements were done at 0T field.

The detectivity was also plotted by dividing our sensor's noise by our previously obtained sensitivity. This needed to be done using the same Ibias used to calculate the MR curve because, for each Ibias value, the sensitivity changes would lead to different detectivity. A new MR curve measurement was performed in the 140 Oe with the corresponding Ibias of the noise setup for each sensor. The full bandwidth ranges from 5 to 100 kHz.

### 6.2.1 Noise level and Detectivity Results for 3D Magnetometer

The 3D Magnetometer was lastly characterized regarding noise. Every direction was characterized individually.

It has been shown that the sensitivity of MTJ's varies according to the introduced bias voltage. It seems that there is a threshold corresponding to a specific bias voltage where the MR slope gets more pronounced and, subsequently, more sensitive [44]. Consequently, after some spectral noise measurements, it was assumed that the bias voltage for our 3D Magnetometer would be around 1,3/1,4 V that is believed to be close to this sensor threshold.

Bellow follows the noise spectrum and detectivity plot measurements from our 3D Magnetometer.

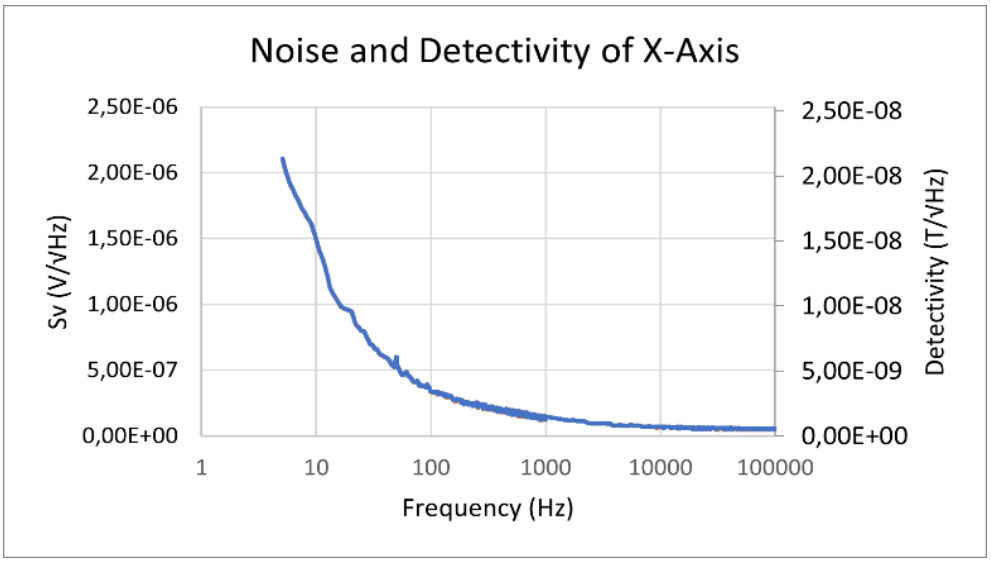


*Figure 37 - X-Axis Spectral Noise and Detectivity*

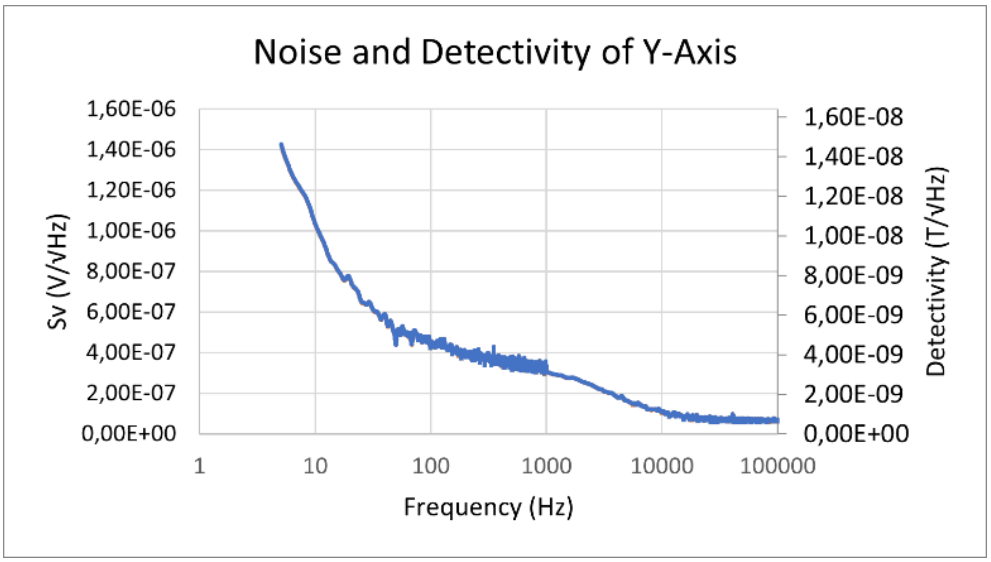


*Figure 38 - Y-Axis Spectral Noise and Detectivity*

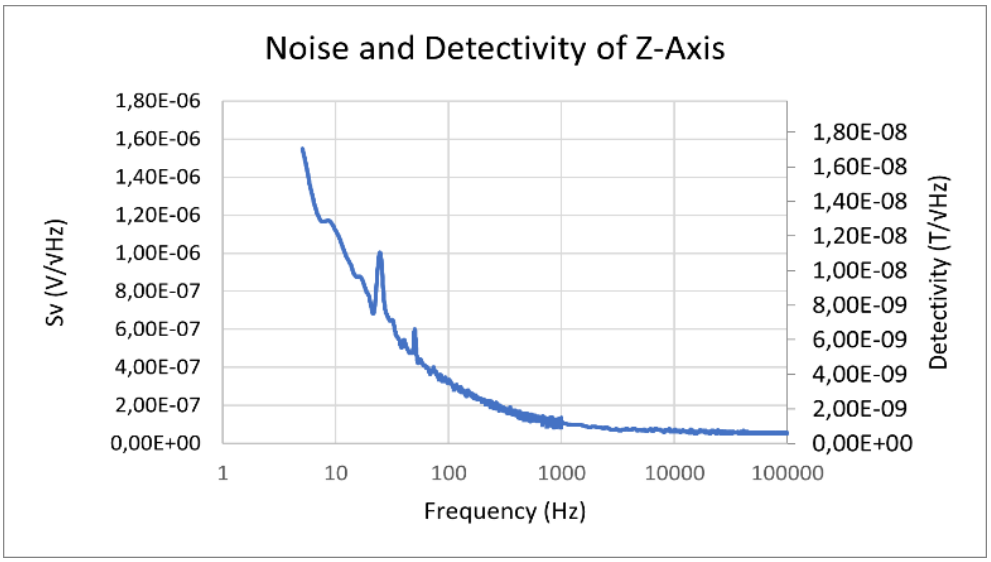


*Figure 39 - Z-Axis Spectral Noise and Detectivity*

Sensors based on an MTJ stack are theoretically dominated at high frequencies by thermal noise, contrasting with the low-frequency regime dominated by 1/f noise.

Here follows a table with our given values for potentiometer resistance, sensor resistance, bias voltage, MR, and a brief sum-up of the detectivity plots.

*Table 6 - Noise 3D Magnetometer Specific Data*

| | X-axis | Y-Axis | Z-Axis |
|---|---|---|---|
| R sensor (KOhm) | 139 | 276 | 182 |
| R potentiometer (KOhm) | 20 | 20 | 20 |
| Vbias (Volt) | 1.38 | 1.4 | 1.5 |
| MR (%) | 40.22 | 39.80 | 40.33 |
| Detectivity (nT/√Hz) @30 Hz | 7.03 | 6.57 | 7.11 |
| Detectivity (nT/√Hz) @1 kHz | 1.31 | 3.43 | 1.17 |

In the low-frequency regime, we can see that we have a similar minimum detectable magnetic field variation. Detectivity levels vary from 6.57 nT/√Hz to 7.11 nT/√Hz, at 30 Hz, for the Y and Z directions, respectively. This is a good outcome to validate this 3D Magnetometer regarding its 3D sensing ability, allowing every axis to be in the same range of detectability, which gives no differential magnetic sensing ability for the Magnetometer and improved full axes coherency.

### 6.2.2 Noise level and Detectivity Results for MTJ 1 and MTJ 2

Bellow follows the noise spectrum and detectivity plot measurements of MTJ 1 and MTJ 2.

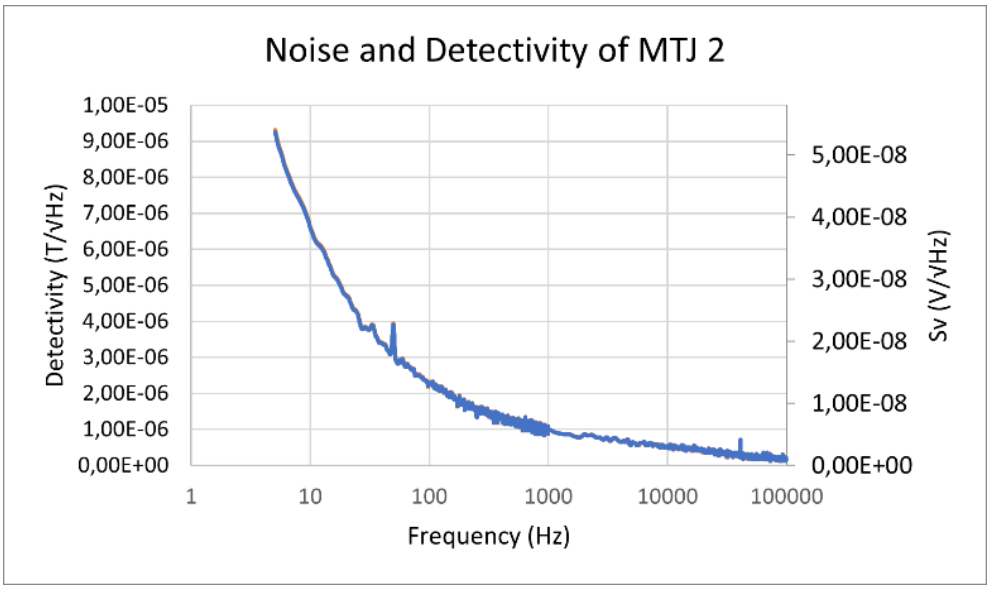


*Figure 40 - MTJ 2 Spectral Noise and Detectivity*

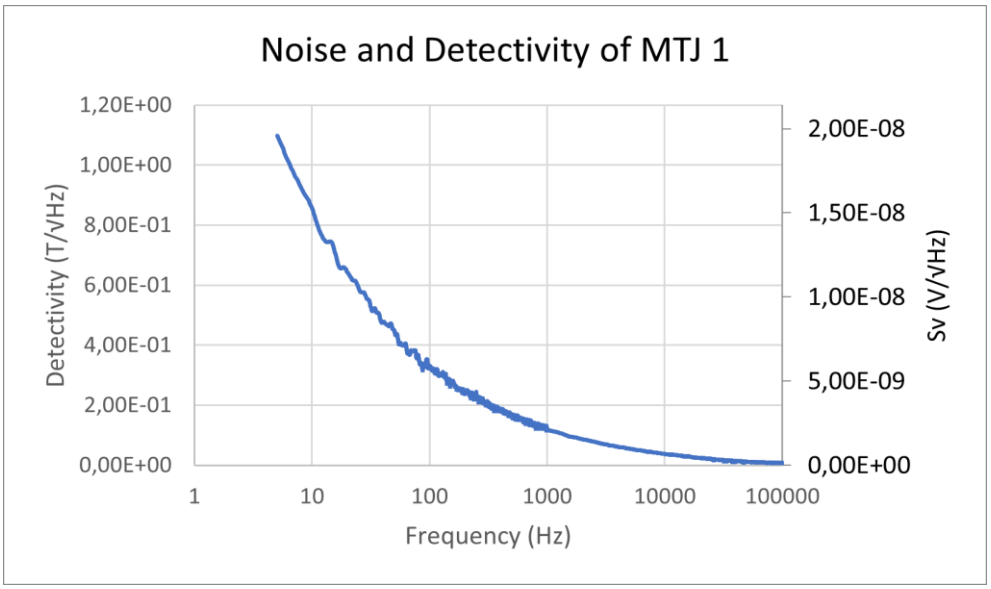


*Figure 41 - MTJ 1 Spectral Noise and Detectivity*

Here follows a table with our given values for potentiometer resistance, sensor resistance, bias voltage, MR and a brief sum-up of the detectivity plots.

*Table 7 - Noise 3D MTJ's Specific Data*

| | MTJ 2 | MTJ 1 |
|---|---|---|
| R sensor (KOhm) | 1673 | 811 |
| R potentiometer (KOhm) | 20 | 20 |
| Vbias (Volt) | 1.48 | 1.35 |
| MR (%) | 59.61 | 76.38 |
| Detectivity (nT/√Hz) @30Hz | 22.01 | 9.86 |
| Detectivity (nT/√Hz) @1 kHz | 5.34 | 2.19 |

We obtained the following detectivity levels in the low-frequency regime, 9.86 nT/√Hz and 22.01 nT/√Hz, at 30 Hz for our MTJ 1 and MTJ 2, respectively.

For these sensors, the ideal Vbias to maximize the sensor's sensitivity was not calculated. This could mean that the detectivity could be even lower, perhaps leading to an even lower detectivity of the one plotted above for the 3D Magnetometer.

### 6.2.3 Noise level and Detectivity Results for Spin-Valve sensors

MTJ's present, in a typical situation, a considerably higher MR ratio than in Spin-Valves, but this comes with a cost of increased intrinsic noise. MTJ offers a great possible alternative to spin-valves if their signal-to-noise ratio surpasses those of spin-valves. The fact that MTJ possesses a higher intrinsic noise is due to several reasons. For instance, above the 1/f knee, one primary source of noise that is present in MR devices is thermal noise. In addition, shot noise becomes a critical key factor in MTJ devices due to the discontinuity in the conduction medium that the MTJ barrier represents. In the low-frequency regime, we also have a more significant contribution of 1/f noise than in spin-valves. In some cases, it can even reach a Hooge parameter 300 times bigger than in spin-valves [45].

The following plots were obtained for our spin-valve sensors.

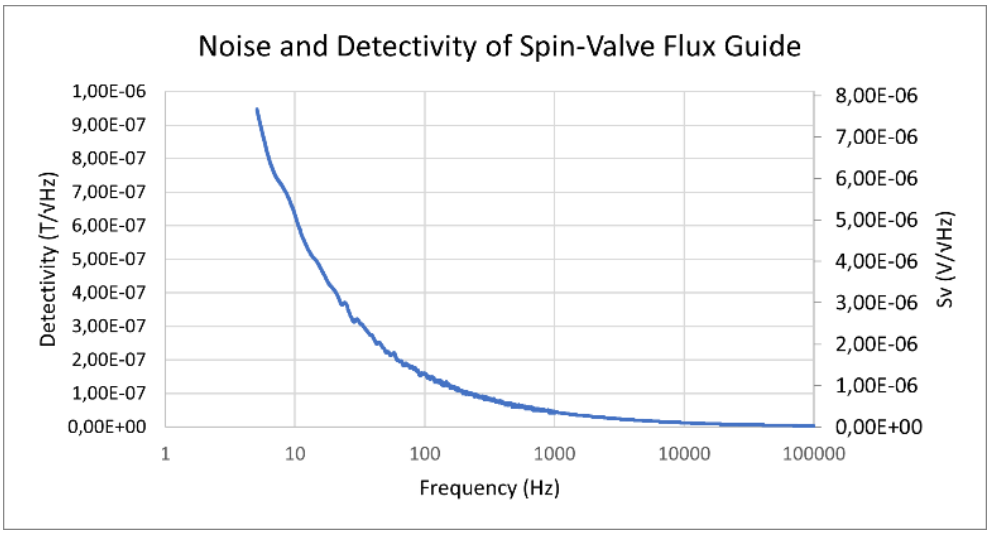


*Figure 43 - Spin-Valve with Flux-Guide Spectral Noise and Detectivity*

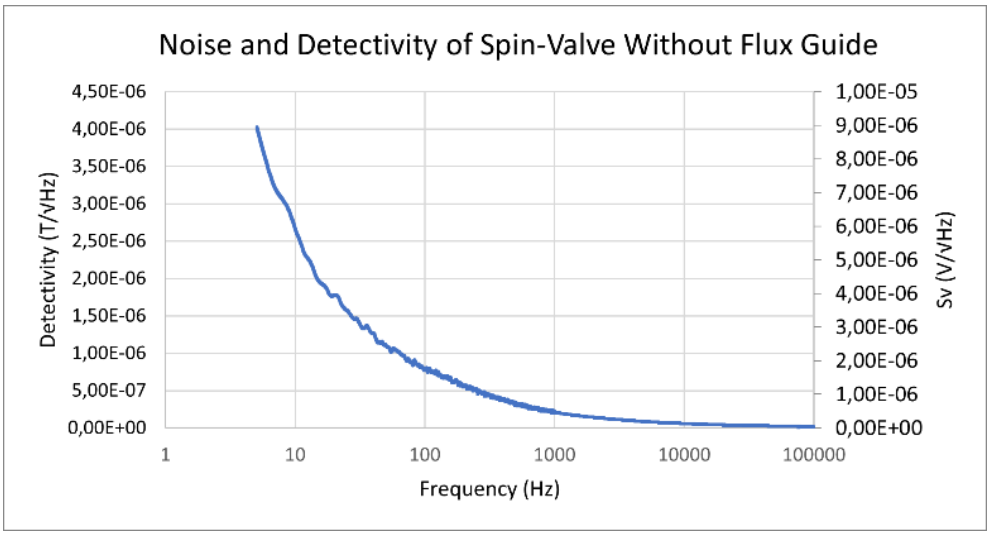


*Figure 42 - Spin-Valve without Flux-Guide Spectral Noise and Detectivity*

Here follows a table with our given values for potentiometer resistance, sensor resistance, bias voltage, MR and a brief sum-up of the detectivity plots.

*Table 8 - Noise Spin-Valve's Specific Data*

| | Flux concentrator | N/ Flux concentrator |
|---|---|---|
| R sensor (Ohm) | 309 | 447 |
| R potentiometer (Ohm) | 512 | 506 |
| Vbias (Volt) | 0.51 | 0.63 |
| MR (%) | 6.53 | 6.68 |
| Detectivity (uT/√Hz) @30Hz | 0.32 | 1.46 |
| Detectivity (nT/√Hz) @1 kHz | 43.94 | 217.62 |

In these Spin-Valves sensors, we can see that the intrinsic sensor noise is similar to our MTJ sensors, which gives our MTJ's a significant competitive advantage regarding detectivity that is enhanced because of MTJ's naturally more considerable sensitivity.

In addition, we can notice a lower Flux concentrator sensor noise compared with the standard spin-valve sensor. This will, in turn, with a more sensitive slope, lead to a detectivity in our Flux concentrator sensor 4,5 times lower than the detectivity of our normal spin-valve, in the low-frequency regime, at 30Hz.

## 6.3 Conclusion

In conclusion, all sensors were successfully characterized regarding MR Curve, Noise Spectrum and Detectivity limits ranging from 5 to 100 Khz.

First, the MTJ that was chosen to build our 3D Magnetometer was not appropriate to the size and power capacity of our 3D Coil Setup. Only part of the linear range was characterized using the coils, developing a 3D Magnetometer unable to be fully characterized with the given Setup. Despite this, the data obtained from both our measured setups was coherent, validating the functionality of both our sensor and our Setup.

Additionally, the characteristics of the MR sensors competing technology for ultra-low field detection has come a long way. From fabrication of single MTJ's, with detectivities ranging from 350 nT/√Hz at 1 Hz

with a 3.3%/Oe sensitivity, to MTJ arrays with more than 1000 junctions, achieving detectivities of 16.2 nT/√Hz at 1 Hz and TMR ratios of 63%, with a device footprint of 0.5x0.5 $mm^2$ [46] [47]. To achieve pT detection levels, some additional fabricating techniques are used. For instance, the use of FM flux-guides integrated into our MTJ, have achieved detectivities of 97 pT/√Hz, at 10 Hz, with sensitivities around 72 %/Oe, with a device footprint of 0.5x0.5 $mm^2$ [48]. Given all these new advances on MR sensors for low field detection, our 3D Magnetometer, composed of a Wheatstone bridge of MTJ's array, with a detectivity at 30 Hz of 7.03, 6.57 and 7.11 nT/√Hz, for the X, Y, and Z-Axis has preeminent abilities. In addition, we obtained a TMR of 59.61% and 76.38%, with a detectivity at 10 Hz of 22.01 nT/√Hz and 9.86 nT/√Hz and a sensitivity of 4.58%/Oe and 1.29%/Oe, for MTJ 2 and MTJ 1, respectively.

Bellow follows a detailed comparation about the sensors described above, as state-of-the art novelty sensors, and sensors produced at INESC-MN.

*Table 9 - Details about state-of-the-art sensors*

| Active Sensor | Details | Detectivity at 1 Hz (T/√Hz) | Device Footprint | MR % | Sensitivity (%/Oe) |
|---|---|---|---|---|---|
| TMR-Single | MTJ | 350.0 nT | N/A | 100% | 3.3%/Oe |
| TMR-Series | MTJ series | 16.2 nT | 0.5x0.5 $mm^2$ | 63% | 3%/Oe |
| TMR-Single | MgO MTJ sensor with Ferromagnetic Flux-Guides | 300.0 pT | 0.5x0.5 $mm^2$ | 100% | 72%/Oe |

*Table 10 - Details about INESC-MN studied sensors*

| Active Sensor | Details | Detectivity at 10 Hz (T/√Hz) | Device Footprint | MR % | Sensitivity (%/Oe) |
|---|---|---|---|---|---|
| TMR-Array | MTJ (X-Axis) | 10.10 nT | 1.00x1.50 $mm^2$ | 40.22% | 0.72 %/Oe |
| TMR | MTJ 1 | 15.10 nT | 0.68x0.40 $mm^2$ | 59.61% | 9.94 %/Oe |
| TMR | MTJ 2 | 38.00 nT | 0.30x0.42 $mm^2$ | 76.38% | 3.47 %/Oe |
| SV-Single | Cu SV sensor with Ferromagnetic Flux-Guides | 0.60 uT | 1.95x1.65 $mm^2$ | 6.53% | 3.27 %/Oe |
| SV-Single | Cu SV sensor | 2.65 uT | 1.70x0.65 $mm^2$ | 6.68% | 0.13 %/Oe |

Both sensors, 3D Magnetometer and MTJ 1 and MTJ 2, present a good competitive profile for low field measurement sensors, regarding detectivity, MR ratio and footprint. Despite this, the measured spin-valves had an intrinsic noise level very similar to the MTJ measured, which did not give rise to a prominent device for low field measurement.

If the 3D Magnetometer were to be rebuilt, we would use the MTJ 1 due to the smaller magnetic linear range, which our sensor can fully characterize, presenting the second smallest detectivity range with the highest MR.

# Chapter 7

## AC magnetic sweep

### 7.1 Sensor Minimum Detectable AC Field Measurement

To test our sensor ability to sense a low-frequency AC magnetic field, we had to create an oscillating magnetic field in our 3D Helmholtz coil and do a magnetic and frequency sweep through our sensor. We assessed its capability to detect a low-frequency magnetic field by calculating measured the sensor noise response's while the AC magnetic field was applied and then calculated the SNR ratio (Speak/Sbackground). The background is the sensor noise signal limit of field detectivity, given by SNR = 1.

This type of experiment is elucidating to understand the limitations in sensor detectivity better and realize if it has any advantage in being used for AC magnetic field detection, such as in healthcare applications. The noise measurements illustrated in the previous chapter define the theoretical prevision of where the sensor noise overcomes the signal response ending our sensor's magnetic sensing. More fit and accurate data can be obtained from the sensors output subjected to a low AC magnetic field due to the actual presence of the magnetic field and not a theoretical prediction at 0 Tesla field.

To generate the oscillating magnetic field, we used our 3D Coil Setup, respectively, the X-axis. The frequency sweep was done from 0 to 100Hz, with the established AC magnetic fields oscillating at a frequency of 10, 20, 40, and 80 Hz. Both sensors and 3D Coil Setup are inside a magnetically shielded box.

The Helmholtz coil was connected to a function generator, and the data was interpreted using the noise setup. For each measurement, 1000 averages were calculated with an RBW of 1.

### 7.1.1 Minimum detectable field for the X-Axis of our 3D Magnetometer

The following plots were obtained for each of the measured frequencies.

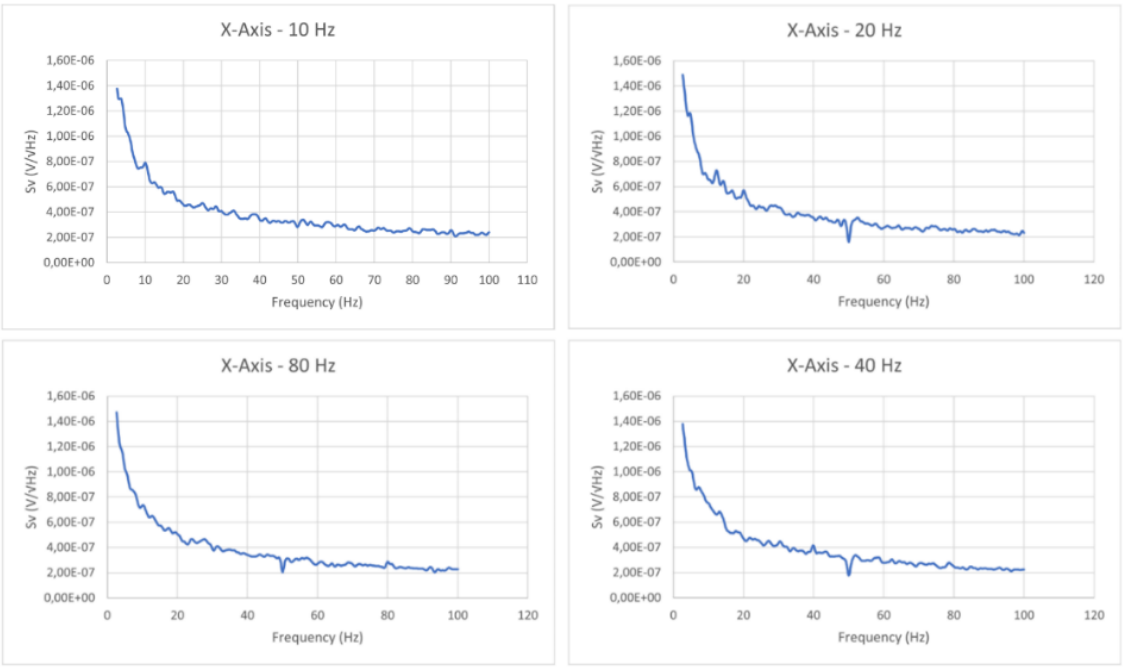


*Figure 44 - AC magnetic field detectivity for low field frequency, respectively, 10, 20, 40 and 80 Hz of X-Axis of 3D magnetometer*

Table 11 – Signal to noise ratio from output signal of our 3D Magnetometer X-Axis

| Frequency (Hz) | Magnetic Field (nT) | SNR |
|---|---|---|
| 10 | 9.73 | 1.05 |
| 20 | 9.73 | 1.10 |
| 40 | 6.33 | 1.13 |
| 80 | 4.14 | 1.23 |

Voltages peaks can be observed from our sensor's output where the AC magnetic field was applied. The estimated root means square value for the measured frequencies, 10, 20, 40, and 80 Hz, is 9.27, 8.85, 5.60, and 3.36 nT for an SNR of 1.

### 7.1.2 Minimum detectable field for MTJ 1 and MTJ 2

The following plots were obtained for each of the measured frequencies:

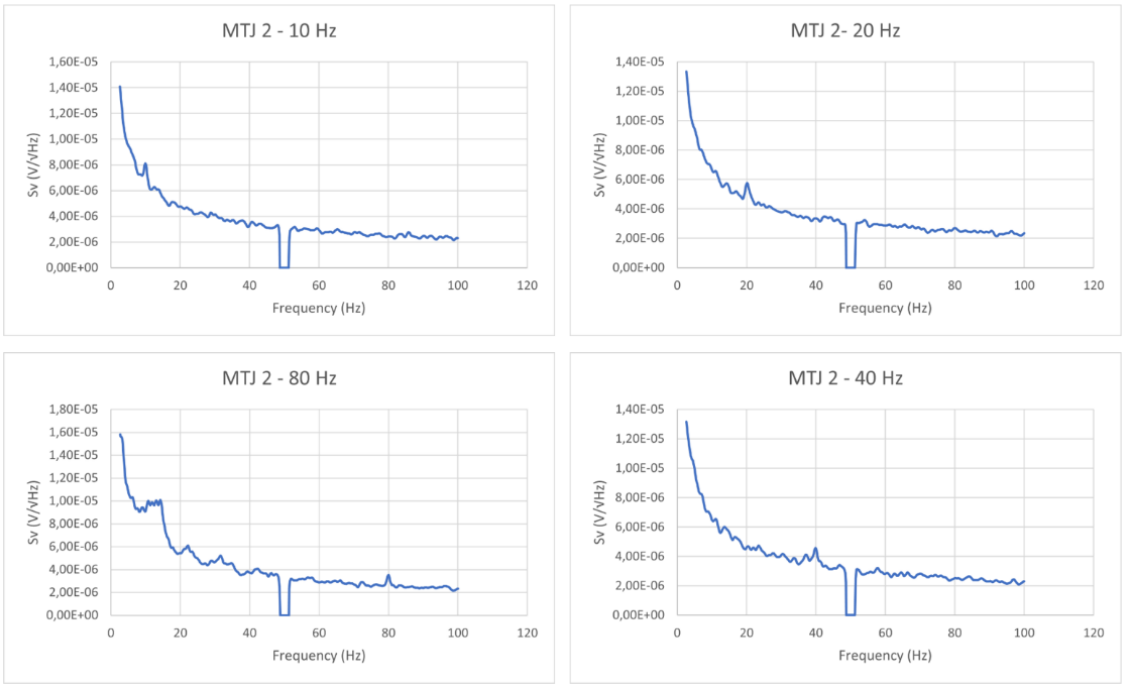


*Figure 45 - AC magnetic field detectivity for low field frequency, respectively, 10, 20, 40 and 80 Hz of MTJ 2*

*Table 12 - Signal to noise ratio from output signal of our MTJ 2*

| Frequency (Hz) | Magnetic Field (nT) | SNR |
|---|---|---|
| 10 | 48.66 | 1.13 |
| 20 | 31.14 | 1.21 |
| 40 | 27.25 | 1.14 |
| 80 | 21.46 | 1.30 |

Voltages peaks can be observed from our sensor's output where the AC magnetic field was applied. The estimated root means square value for the measured frequencies, 10, 20, 40, and 80 Hz, is respectively, 43.06, 25.74, 23.90, and 16.50 nT for an SNR of 1.

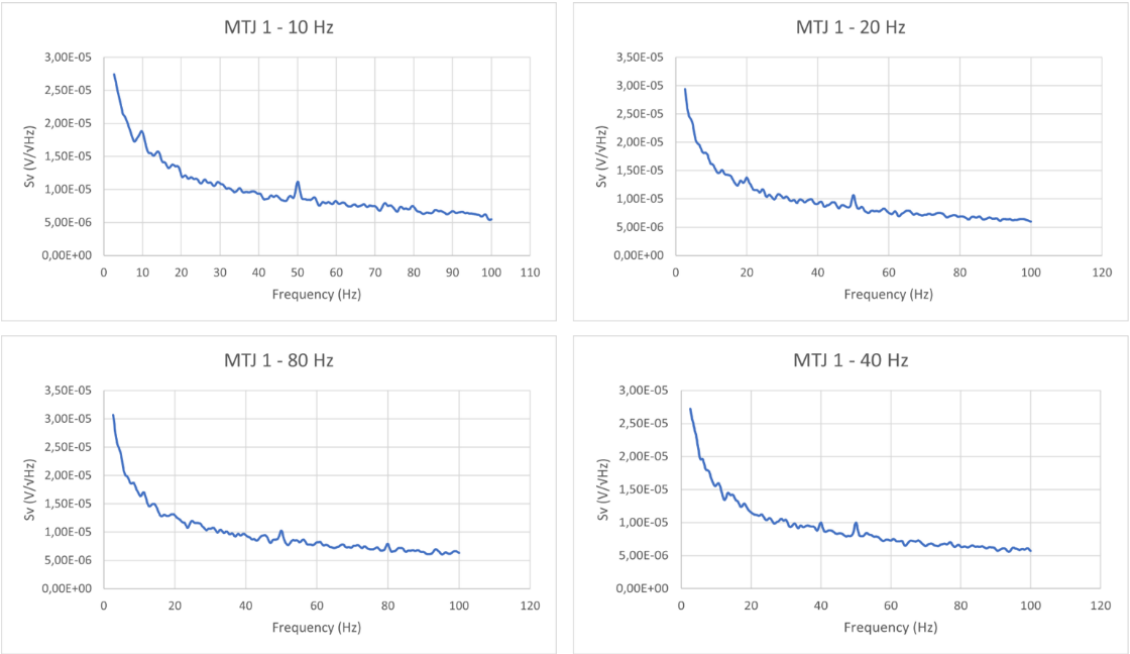


*Figure 46 - AC magnetic field detectivity for low field frequency, respectively, 10, 20, 40 and 80 Hz of MTJ 1*

*Table 13 - Signal to noise ratio from output signal of our MTJ 1*

| Frequency (Hz) | Magnetic Field (nT) | SNR |
|---|---|---|
| 10 | 22.38 | 1.02 |
| 20 | 19.46 | 1.06 |
| 40 | 19.46 | 1.13 |
| 80 | 15.57 | 1.14 |

Voltages peaks can be observed from our sensor's output where the AC magnetic field was applied. The estimated root means square value for the measured frequencies, 10, 20, 40, and 80 Hz, is 21.94, 18.36, 17.22, and 13.66 nT for an SNR of 1.

### 7.1.3 Minimum detectable field for Spin-Valve sensors

The following plots were obtained for each of the measured frequencies.

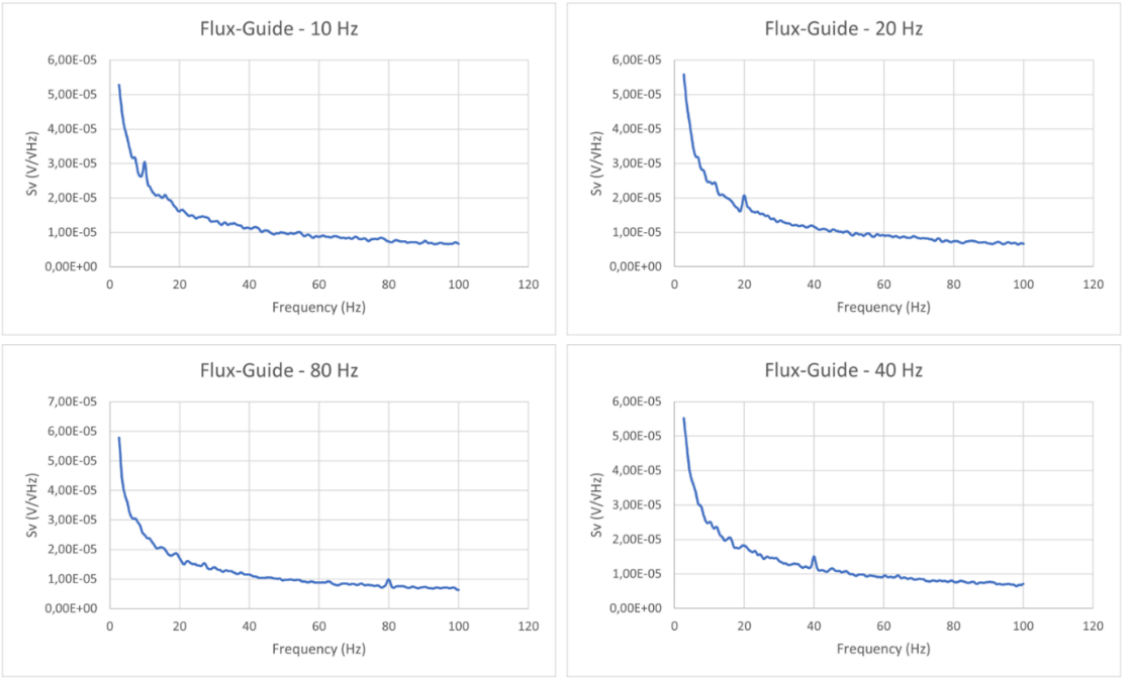


*Figure 47 - AC magnetic field detectivity for low field frequency, respectively, 10, 20, 40 and 80 Hz of Spin-Valve Flux-Guide*

*Table 14 - Signal to noise ratio from output signal of our Spin-Valve Flux-Guide*

| Frequency (Hz) | Magnetic Field (uT) | SNR |
|---|---|---|
| 10 | 88.48 | 1.16 |
| 20 | 53.09 | 1.23 |
| 40 | 42.24 | 1.27 |
| 80 | 26.54 | 1.24 |

Voltages peaks can be observed from our sensor's output where the AC magnetic field was applied. The estimated root means square value for the measured frequencies, 10, 20, 40, and 80 Hz, is 76.28, 43.16, 33.25, and 21.40 uT for an SNR of 1.

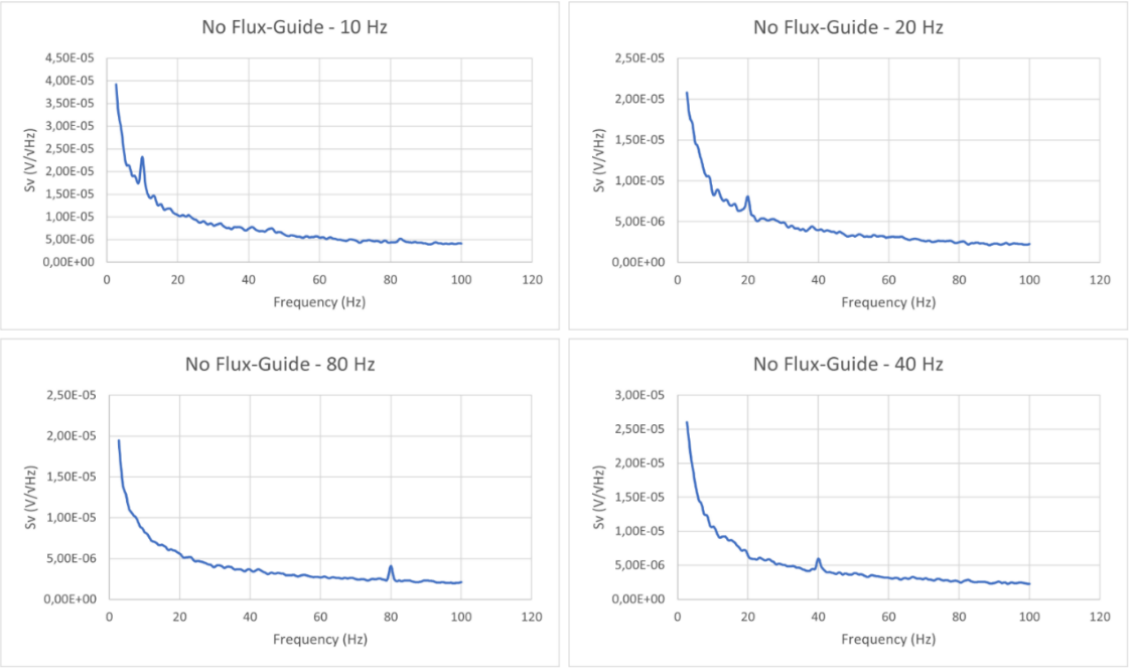


*Figure 48 - AC magnetic field detectivity for low field frequency, respectively, 10, 20, 40 and 80 Hz of Spin-Valve without Flux-Guide*

*Table 15 - Signal to noise ratio from output signal of our Spin-Valve without Flux-Guide*

| Frequency (Hz) | Magnetic Field (uT) | SNR |
|---|---|---|
| 10 | 115.01 | 1.32 |
| 20 | 79.63 | 1.19 |
| 40 | 61.93 | 1.34 |
| 80 | 53.09 | 1.6 |

Voltages peaks can be observed from our sensor's output where the AC magnetic field was applied. The estimated root means square value for the measured frequencies, 10, 20, 40, and 80 Hz is respectively, 87.13, 66.92, 46.22, and 33.18 uT for an SNR of 1.

## 7.2 Conclusion

All our sensors could detect a low-frequency magnetic field and were characterized regarding detectivity limits in the low-frequency field compartment, providing an excellent readout of the sensor's detective capacity and consequently increasing our sensor's panorama comprehension.

These measurements were done with an RBW of 1 and 1000 measured averages, which gently improves the noise spectrum accuracy by not doing the measurements at 0 T field, values of which, we can now compare to.

*Table 16 - Theoretical Detectivity Limits vs Measured Detectivity Limits*

| | Measured Detectivity @10Hz | Theoretical Detectivity @10Hz |
|---|---|---|
| X-Axis Sensor | 9.27 nT | 10.05 nT |
| MTJ 1 | 21.94 nT | 10.67 nT |
| MTJ 2 | 43.06 nT | 26.87 nT |
| Spin-Valve Flux-Guide | 76.28 uT | 442.64 nT |
| Spin-Valve Without Flux Guide | 87.13 uT | 1.87 uT |

We can see that, except for the X-Axis sensor, all the other values were above the minimum detectable magnetic field oscillation. That is one of the key factors of having this type of sensor characterization, leading to more accurate data that can better define our sensing device.

In addition, the spin-valve sensors were the ones that had the biggest disparity between theoretical detectivity limitations and actual calculated values, having a minimum detectivity 172 and 46 times bigger than the expected one, for Spin-Valve with and without Flux-Concentrator, respectively.

The difference in these values is mainly related to applying an external magnetic field that will shift and generate more magnetic 1/f noise. Another reason was that the Vbias introduced into our sensors was not the same from this and the previous measurements, changing the sensitivity and consequently the detectivity. This happened because of a problem in the potentiometer from the noise Setup, which disabled us from having the same consistent Vbias.

# Chapter 8

## Flux concentrator MR Characterization with cross-field

### 8.1 Linearization Strategy

To promote sensor linearization, several techniques can be employed. One of them can be to apply an external permanent magnetic field in the transversal sensing direction. This effect can diminish the effect of a coercive MR curve and consequently suppress some of the hysteresis [49] [50] [51]. In this experiment, we took our more sensitive sensor, which is respectively, the Flux concentrator Spin-Valve sensor, and measured different MR curves with different cross magnetic external fields.

For this purpose, we used our 3D Coil Setup to measure the MR curve of our sensor with its easy axis in the X-axis and applied the external magnetic field in the Y-direction.

The following plots were obtained.

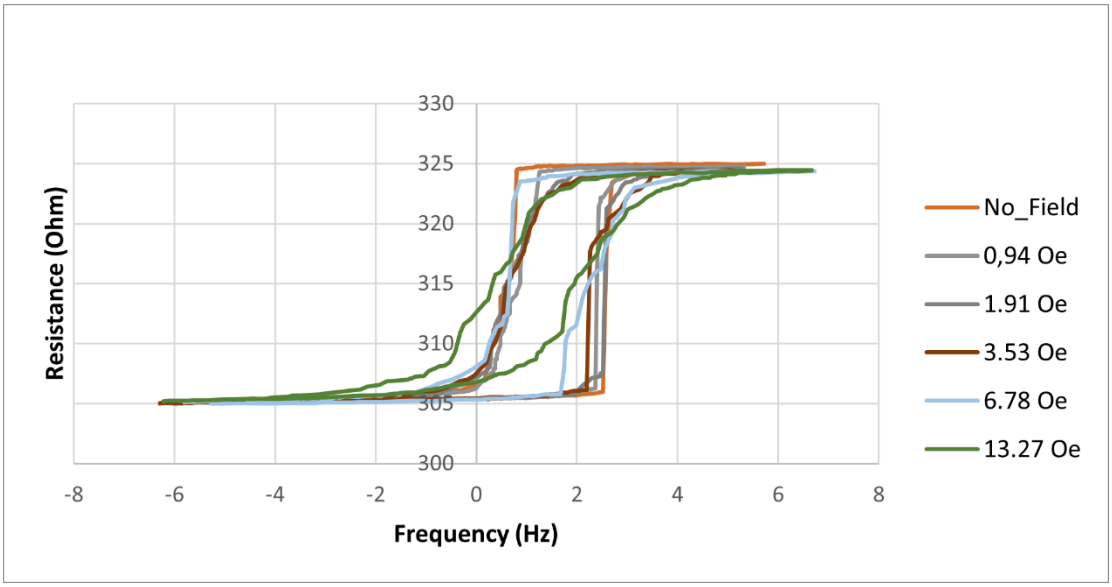


*Figure 49 - Effect of crossed applied magnetic field on magnetoresistive curve of the Spin-Valve with Flux-Guide sensor*

*Table 16 - Sensitivity and Coercivity for each of the crossed magnetic fields applied*

| Magnetic Field (Oe) | Sensitivity (Ohm/Oe) | Coercivity (Oe) |
|---|---|---|
| No_Field | 63.31 | 1.92 |
| 0.94 | 23.44 | 1.67 |
| 1.91 | 18.87 | 1.80 |
| 3.53 | 11.01 | 1.66 |

| | | |
|---|---|---|
| 6.78 | 8.87 | 1.57 |
| 13.28 | 4.35 | 1.36 |

We can see a shift towards sensor linearization, with a decrease in the hysteric curve and sensitivity. The coercivity in the final MR measurement, 13.28 Oe, had a 30% reduction, a considerable coercive loss from 1.92 Oe to 1.36 Oe. In addition, the sensitivity had a reduction of 93%, going from a very steep linear range to a softer curve.

This linearization effect is given by the following equation [48]

$$\frac{E_{bias}^{sen}}{V^{sen}} = \mu_0 M_s^{sen} H_{bias} sin\theta \quad (19)$$

Where $\mu_0$ is the vacuum permeability constant, $M_s^{sen}$ the magnetization of the sensing layer, $H_{bias}$ bias external field and $\theta$ is the angle between the crossed magnetization and the sensing direction.

Taking this equation and joining it with this experiment, we can understand that by increasing the crossed magnetic external field, there will be a threshold ($\mu_0 H_{bias}$) defining the transition from a hysteric curve to a linear sensing curve. In our case, this threshold is 13.28 Oe, where the coercivity becomes lower and the sensing curve more linear. This loss of coercivity comes with losing our sensor sensitivity, which will increase our detectivity limit.

Permanent magnets are sometimes used for this type of linearization strategy. In this scenario, permanent magnets can be replaced by a portable 3D Setup Coil that can be tuned according to the specific MR sensor to the desired magnetic field.

# Chapter 9

## Conclusion

The main objective of this Thesis was to successfully build a 3D magnetometer with a size no bigger than 100 $\mathrm{mm}^2$ and with the final device dimension no bigger than 25 $\mathrm{cm}^2$. Parallelly with the developing of a fully functional 3D Setup Coil system to characterize the respective magnetometer and a specific dataset of low field MR sensors.

A successful 3D magnetometer was mounted on a QFN chip carrier where the Z-axis was integrated vertically into our chip carrier by manipulating the sensor during the wire bonding procedure.

Meanwhile, the 3D Coil Setup was also successfully built in the INESC-MN 3D printer. All the coil parameters were finely tuned regarding the specific desires for the 3D Coil Setup, such as sensitivity, uniformity, minimum induced magnetic field, and device compactness. We were able to produce a setup with approximately 0.2 $m^2$, high field uniformity and the possibility of producing 1 pT of induced magnetic field with 1 nA of coils current. These values were calculated according to INESC-MN's current source. For each sensing axis, calibration was done, which produced an 8%, 3.5%, and 5% referential difference from the calculated theoretical slope regression curve for X, Y, and Z-Axis, respectively.

After successfully implementing these two assembled devices, the next step was to characterize the assembled sensors dataset, including the 3D Magnetometer, using the 3D Coil Setup.

All sensors were characterized using the 3D Coil Setup and plotted against reference values obtained in the 140 Oe setup. Despite some data disparity, all the MR curves were coherent and consistent with the obtained data. The MR curve for our 3D Magnetometer led to a sensitivity percentual difference, in the linear range, of 8%, 3%, and 6% for X, Y, and Z-Axis, respectively. For the Spin-Valve sensors, we obtained a magnetoresistance deviation of 6.5% and 2.4% for the Flux concentrator and No Flux concentrator sensors, respectively. Regarding MTJ's given by INESC-MN, they had a magnetoresistance deviation from the reference values of 1% for the MTJ 1 and MTJ 2.

The existing data disparity could be improved by a script alteration that would take several measures from the voltmeter, considering the measured average of them all. Another annotation would be to draw in SolidWorks a new piece that could be integrated into the 3D Coil Setup to lock the sensor in the geometrical coil center. One final annotation was the number of measurements done in the 140 Oe, that for a more sensitive slope, would need a different number of measured points in the sensitive area to produce a more accurate MR curve.

Regarding noise characterization of our 3D Magnetometer, we obtained final detectivities with a maximum 7.5% disparity between them, allowing every axis to be in the same range of detectability, which gives no differential magnetic sensing ability for the Magnetometer and improved whole axis coherency.

Additionally, we created a low-frequency AC magnetic field to assess our sensor's capability of detecting fields in the 1/f dominated area. After measuring the SNR ratio of our output signal according to a specific created magnetic field, we could infer detectivity limits for each frequency. The Flux concentrator sensor detected an AC magnetic field of 88.48 uT at 10 Hz, while the non-flux concentrator sensor was slightly above that value, with 115.01 uT at 10 Hz. Both MTJ sensors provided by INESC-MN, at 10 Hz, were able to detect an AC magnetic field of 48,66 nT and 22,38 nT, for MTJ 2 and MTJ 1. The sensor with the best detectivity at 10 Hz was the MTJ used from our 3D Magnetometer, with a 9.73 nT magnetic field detection at 10 Hz.

Both sensors, 3D Magnetometer and MTJ 1 and MTJ 2, present a good competitive profile for low field measurement sensors. Despite this, the measured spin-valves had an intrinsic noise level very similar to the MTJ measured, which did not give rise to a prominent device for low field measurement. In addition, the spin-valve sensors were the ones that had the biggest disparity between theoretical detectivity limitations and actual calculated values, having a minimum detectivity 172 and 46 times bigger than the expected one, for Spin-Valve with and without Flux-Concentrator, respectively.

Furthermore, an experiment was done to study the implications of cross-applied magnetic fields in the MR curve of MR sensors. For this purpose, we used the 3D Magnetic Coil setup to generate the cross magnetic field while leaving the other in-plane orthogonal axis for sensing. From a 0 Oe first measurement to an applied 13.2 Oe, we observed a decrease of 30% and 93% in coercivity and sensitivity, respectively. Concluding, this type of strategy has beneficial implications in MR sensors linearization strategies.

Moreover, if the 3D Magnetometer were to be rebuilt, we would use the MTJ 1 due to the smaller magnetic linear range, which our sensor can fully characterize, presenting the second smallest detectivity range with the highest MR.

In conclusion, a compact, sensitive, and accurate 3D Coil Setup was built and provided several characterization measurements of a set of MR sensors. This Setup is highly portable, leading to some noise and detectivity measurements that would not be possible to address beforehand. All future 3D Magnetometers will have the possibility of having every sensing axis characterized in the same device without changing the given sensor position. Finally, the possibility of being used as a tool for linearization strategies was demonstrated. Accounting for the Setup Portability, it could be a valuable asset given that the Magnetic Field can be tuned according to every sensor's need instead of using a permanent magnet.

# References


[1] C. H. Bajorek, "Magnetoresistive (MR) Heads and the Earliest MR Head-Based Disk Drives: Sawmill and Corsair," *Storage Special Interest Group,* p. 10, 29 05 2015.

[2] P. Gokhale..US Patent 4,835,467, 1989.

[3] J. Valadeiro, "Magnetoresistive sensors with pico-tesla sensitivities," . *Master's thesis, Instituto Superior Tecnico,* 2014.

[4] J. Hu, M. Pan, J. Hu, S. Li, D. Chen, W. Tian, K. Sun, Q. Du, Y. Wang, L. Pan, W. Zhou, Q. Zhang, P. Li, J. Peng, W. Qiu and J. Zhou, "Resolution improvement of low frequency AC magnetic field modulated MR sensors," *REVIEW OF SCIENTIFIC INSTRUMENTS,* vol. 88, p. 095006, 2017.

[5] S. J. Han, "CMOS Integrated DNA Microarray Based on GMR Sensors," *Stanford University,* 2007.

[6] Y. Nagano, "Early history of sudden commencement investigation and some newly discovered historical facts," *Hist. Geo Space. Sci.,* vol. 12, no. 2, pp. 131-162, 2021.

[7] J. Lenz and A. Edelstein, "Magnetic Sensors and Their Applications. Sensors," *IEEE,* vol. 6, pp. 631-649, 2006.

[8] P. Ripka, "Magnetic Sensors and Magnetometers," *Artech House,* 2001.

[9] A. Marcellis, "Giant Magnetoresistance (GMR) sensors for 0.35µm CMOS technology sub-mA current sensing,," *IEEE,* pp. 444-447, 2014.

[10] J. Kubik, M. Vopalensky and P. Ripka, "Precise amr magnetometer for compass,," *IEEE,* vol. 1, pp. 472-476, 2003.

[11] N. Smith, F. Jeffers and J. Freeman, "A high-sensitivity magnetoresistive magnetometer.,," *J. Appl. Phys.,* vol. 69, no. 5082, 1991.

[12] R. Waser, Nanoelectronics and Information Technology: Advanced Electronic Materials and Novel, Germany, 2012.

[13] S. Cardoso and C. Reig, "Giant Magnetoresistance (GMR) Sensors," *Smart Sensors, Measurement and Instrumentation,* vol. 6, 2013.

[14] M. Díaz-Michelena, "Small magnetic sensors for space applications.,," *Sensors,* vol. 9, pp. 2271-88, 2009.

[15] S. Parkin, C. Kaiser, A. Panchula, P. Rice, B. Hughes, M. Samant and S. Yang, "Giant tunnelling magnetoresistance at room temperature with mgo (100) tunnel barriers.,," *Nature Materials,* vol. 12, no. 3, pp. 862-867, 2004.

[16] S. Yuasa, T. Nagahama, A. Fukushima, Y. Suzuki and K. Ando, "Giant room- temperature magnetoresistance in single-crystal fe/mgo/fe magnetic tunnel junctions.,," *Nature Materials,* vol. 12, no. 3, pp. 868-871, 2004.

[17] S. Ikeda, J. Hayakawa, Y. Ashizawa, Y. Lee, K. Miura, H. Hasegawa, M. Tsunoda, F. Matsukura and H. Ohno, "Tunnel magnetoresistance of 604suppression of ta diffusion in cofeb/mgo/cofeb pseudo spin-valves annealed at high temperature.,," *Applied Physics Letters,* vol. 8, no. 93, 2008.

[18] X. Yin, R. Skomski, D. Sellmyer, S. Liou, S. Russek, E. Evarts, J. Moreland and A. Edelstein, "Adjusting magnetic nanostructures for high-performance magnetic sensors," *Journal of Applied Physics,* vol. 115, no. 17, p. 17E528, 2014..

[19] S. Cardoso, D. C. Leitao, L. Gameiro, F. Cardoso, R. Ferreira, E. Paz and F. P., "Microsystem technologies," *Magnetic tunnel junction sensors with pTesla sensitivity,* vol. 20, no. 4-5, pp. 793-802, 2014.

[20] J. Teixeira, J. Ventura, M. Fernández-García, J. Araujo, J. Sousa and W. P. Leitao, "Exchange biased CoFeB-MgO tunnel junctions at the onset of perpendicular anisotropy with in-plane/out-of-plane sensing capabilities," *Journal of Applied Physics,* vol. 111, no. 5, p. 053930, 2012.

[21] J. M. Teixeira, J. Ventura, M. P. Fernandez-Garcia, J. P. Araujo and J. B. Sousa, "Exchange biased CoFeB-MgO tunnel junctions at the onset of perpendicular anisotropy with in-plane/out-of-plane sensing capabilities," *Exchange biased CoFeB-MgO tunnel junctions at the onset of perpendicular anisotropy with in-plane/out-of-plane sensing capabilities,* vol. 111, p. 053930, 2012.

[22] Y. Chao, "Magnetic tunnel junction based out-of-plane field sensor with perpendicular magnetic anisotropy in reference layer," *Journal of Applied Physics,* vol. 117, no. 17, p. 17A320, 2015.

[23] Z. Lei, S. Yan, Z. Cao, Z. Guo, P. Song, Y. Qiang, J. Wang, W. Zhao and Q. Leng, "High TMR for both in-plane and perpendicular magnetic field justified by CoFeB free layer thickness for 3-D MTJ sensors," *AIP Advances,* vol. 9, p. 085127, 2019.

[24] V. Luong, J. Jeng, B. Lai, J. Hsu, C. Chang and C. Lu, "Design of 3-D Magnetic Field Sensor With Single Bridge of Spin-Valve Giant Magnetoresistance Films," *IEEE Transactions on Magnetics,* vol. 51, no. 11, pp. 1-4, 2015.

[25] J. G. Deak, "Practical Tunneling Magnetoresistive Z-Axis Sensors," *AMA Conferences,* p. 6, 2015.

[26] T. McGuire, "Anisotropic magnetoresistance in ferromagnetic 3d alloys," *IEEE Transactions on Magnetics,* vol. 11, no. 4, p. 1018–1038, 1975.

[27] R. Ferreira, "Ion Beam Deposited Magnetic Spin Tunnel Junctions targeting HDD Read Heads, Non-volatile Memories and Magnetic Field Sensor Applications," *PhD thesis,* 2008.

[28] R. E. Peierls, "Quantum Theory of Solids," *Oxford,* 1955.

[29] S. Shen, P. Ohodnicki, S. Kernion and M. McHenry, "Two-current model of the composition dependence of resistivity in amorphous (Fe100− xCox) 89− yZr7B4Cuy alloys using a rigid-band assumption.," *Journal of Applied Physics,* vol. 112, p. 103705, 2012.

[30] V. S. Speriosu, S. S. Parkin, B. A. Gurney, D. R. Wilhoit and D. Mauri, "Giant magnetoresistive in soft ferromagnetic multilayers," *Phys. Rev.,* vol. 43, pp. 1297-1300, 1991.

[31] G. Binasch, P. Grunberg, F. Saurenbach and W. Zinn, "Enhanced magnetoresistance in layered magnetic-structures with antiferromagnetic interlayer exchange,," *Physical Review,* vol. 39, no. 7, p. 4828–4830, 1997.

[32] O. N. Mryasov, P. R. LeClair and E. Y. Tsymbal, "Spin-dependent tunneling in magnetic tunnel junctions," *Journal of Physics,* vol. 15, no. 4, pp. 109-142, 2003.

[33] M. Veigas, "Optimization of magnetoresistive sensors for high power," *Master Thesis Instituto Superior Técnico,* 2018.

[34] A. Friedel and J. Blandin, "Propriétés magnétiques des alliages dilués. Interactions magnétiques et antiferromagnétisme dans les alliages du type métal noble-métal de transition," *J. Phys. Radium,* vol. 20, no. 2-3, pp. 160 - 168, 1959.

[35] L. A. Francis, K. Poletkin and K. Iniewski, "Magnetic Sensors and Devices," *Technologies and Applications,* 2017.

[36] P. Freitas, R. Ferreira, S. Cardoso and F. Cardoso, "Magnetoresistive sensors," *Journal of Physics: Condensed Matter,* vol. 19, no. 16, p. 165221, 2007.

[37] P. P. Freitas, R. Ferreira, S. Cardoso and F. Cardoso, "Magnetoresistive sensors," *J. Phys.: Condens. Matter,* vol. 19, p. 165221, 2007.

[38] H. Nyquist, "Thermal agitation of electric charge in conductors,," *Physical Review,* vol. 32, no. 1, pp. 110-113, 1928.

[39] J. B. Johnson, "Thermal agitation of electricity in conductors,," *Physical Review,* vol. 32, no. 1, pp. 97-109, 1928.

[40] C. Ren, X. Liu, B. Schrag and G. Xiao, "Low-frequency magnetic noise in magnetic tunnel junctions.," *Physical Review,* vol. 69, no. 10, p. 104405, 2004.

[41] R. Guerrero, M. Pannetier-Lecoeur, C. Fermon, S. Cardoso, R. Ferreira and P. P. Freitas, "Low frequency noise in arrays of magnetic tunnel junctions connected in series and parallel," *Journal of Applied Physics,* vol. 105, p. 113922, 2009.

[42] W. Franzen, "Generalization of UniformMagnetic Fields by Means of Air Core Coils," *Review of Sci Inst.,* vol. 33, no. 9, p. 933, 1962.

[43] D. S. Batista, F. Granziera, M. C. Tosin and L. F. d. Melo, "Three-Axial Helmholtz Coil Design and Validation for Aerospace Applications," *IEEE Transactions on Aerospace and Electronic Systems,* vol. 54, no. 1, pp. 392-403, 2018.

[44] P. Wiśniowski, M. Nawrocki, J. Wrona, S. Cardoso and P. P. Freitas, "Bias Voltage Dependence of Sensing Characteristics in Tunneling Magnetoresistance Sensors," *Sensors,* vol. 21, no. 7, pp. 1424-8220, 2021.

[45] W. Weitensfelder, H. Brueckl, A. Satz, K. Pruegl, J. Zimmer, S. Luber, W. Raberg, C. Abert, F. Bruckner, A. Bachleitner-Hofmann, R. Windl and D. Suess, "Comparison of Sensitivity and Low Frequency Noise Contributions in GMR and TMR Spin Valve Sensors with a Vortex State Free Layer," *Phys. Rev.,* vol. 10, no. 5, p. 054056, 2018.

[46] D. Mazumdar, X. Liu, B. D. Schrag, W. Shen, M. Carter and G. Xiao, "Thermal stability, sensitivity, and noise characteristics of MgO-based magnetic tunnel," *Journal of Applied Physics,* vol. 101, p. 09B502, 2007.

[47] R. Guerrero, M. Pannetier-Lecoeur, C. Fermon, S. Cardoso, R. Ferreira and P. P. Freitas, "Low frequency noise in arrays of magnetic tunnel junctions connected in series and," *Journal of Applied Physics,* vol. 105, no. 11, p. 113922, 2009.

[48] R. C. Chaves, P. P. Freitas, B. Ocker and W. Maass, "Low frequency picotesla field detection using hybrid MgO based tunnel sensors.," *Applied Physics Letters,* vol. 91, no. 10, p. 102504, 2007.

[49] F. Jeffers, J. Freeman, R. Toussaint, N. Smith, D. Wachenschwanz, S. Shtrikman and W. Doyle, "A specific model for domain-wall nucleation in thin-film Permalloy microelements," *IEEE Trans. Magn.,* vol. 21, p. 1563, 1985.

[50] K. Yamada, "Shielded magnetoresistive head for high density recording,," *IEEE Transactions on Magnetics,* vol. 26, no. 6, pp. 3010-3015, 1990.

[51] M. Kitada, Y. Kamo and H. Tanabe, "Magnetoresistive thin-film sensor with permanent magnet biasing film," *Journal of Applied Physics,* vol. 58, pp. 1667-1670, 1985.